

High Fidelity Freeform Manufacturing via Polyspectral Tomographic Reconstruction

Bin Wang¹, Weichao Sun^{2,3}, Hossein S. Mozajin², Jadze P. C. Narag⁴, Thor D. V. Christiansen⁵, Adrian A. Schiefler⁶, Jeppe R. Frisvad⁵, Henning O. Sørensen^{6,7}, Kristoffer Almdal², Aminul Islam¹, Yi Yang^{2,8*}

Affiliations:

¹ Department of Mechanical Engineering, Technical University of Denmark; 2800 Kongens Lyngby, Denmark.

² Department of Chemistry, Technical University of Denmark; 2800 Kongens Lyngby, Denmark.

³ PERFI Technologies, ApS; 2800 Kongens Lyngby, Denmark.

⁴ Department of Health Technology, Technical University of Denmark; 2800 Kongens Lyngby, Denmark.

⁵ Department of Applied Mathematics and Computer Science, Technical University of Denmark; 2800 Kongens Lyngby, Denmark.

⁶ Department of Physics, Technical University of Denmark; 2800 Kongens Lyngby, Denmark.

⁷ Xnovo Technology ApS, 4600 Køge, Denmark.

⁸ Center for Energy Resources Engineering, Technical University of Denmark; 2800 Kongens Lyngby, Denmark.

*Corresponding author. Email: yyan@dtu.dk

Abstract

A key goal of freeform manufacturing is to achieve speed, precision and design freedom at the same time. Volumetric additive manufacturing via tomographic reconstruction offers high speed but cannot achieve optical resolution at high design freedom. Here we combine polyspectral tomographic reconstruction with pseudo-negative illumination to resolve the trilemma. We used the same units on a digital micromirror device to modulate two colors of illumination simultaneously to control the chemical stability of binary photoinhibition. The methodology enables a typical 4K projector to 3D-print up to 8.9 billion voxels in a $\text{Ø}30\times 50$ mm vial at two-digit-m-resolution in minutes, with prolonged process window and geometrically fidelous greyscale printing. These results are linked to, and thus can be improved directly upon upgrading, the precision of the optomechanical modality.

One-Sentence Summary: Key milestones in freeform manufacturing trilemma reached simultaneously via polyspectral tomographic reconstruction.

Main Text:

Naturally occurring, hierarchically branched structures stemming from self-organization of solid-fluid interactions have long been an inspiration for the design of artificial machinery and devices (1). To experimentally investigate the efficiency of resource collection and distribution via branching structures, a freeform manufacturing technique is needed to fabricate such multiscale architecture in 3D. An ideal technique tackles the *speed-precision-design freedom* triangle, i.e., strives to accurately deliver an object with complex geometry at high speed. The availability of such a technique will pave the way for building groundbreaking use cases such as fully vascularized artificial tissues or organs (2). Progress in tackling the “impossible triangle” can be marked by three key milestones. For *design freedom*, one strives to realize greyscale printing of any geometry. For *precision*, one expects to establish a clear relationship between the fabrication resolution and optomechanical resolution, so that manufacturing could benefit directly from upgrading the modality. For *speed*, one aims to sever the link between required time and design complexity, attaining an inherent dimensionality of three. Computed axial lithography (CAL), also known as tomographic volumetric printing (TVP) (3-5), builds an object by projecting patterned illumination upon a curing volume from different angles. The imaginary dose buildup is coupled with photoresponses to solidify all points in a workpiece in parallel, and is currently the only inherently three-dimensional freeform manufacturing technique for non-periodical structures. Remarkable progress has been made in developing CAL/TVP in recent years, extending its applicability to a wide spectrum of materials and applications, and smallest reproducible features spanning between 20 to 80 μm have been reported (see refs (6, 7) and therein). However, four fundamental concerns remain. First, when reporting a feature size, does it reflect the fabrication resolution in the axial direction or on the lateral plane. In conventional

digital light processing (DLP)-based vat photopolymerization (VPP), horizontal and vertical fabrication resolutions are reported separately, as the former correlates directly with the optical resolution of the modality on the focal plane, while the latter is further impacted by factors such as motorization and fluid flow. In TVP, although the chemical coupling is identical for both vertical and lateral planes, there is a clear disparity between the corresponding fabrication resolutions. The relationship between the vertical resolution and the optical resolution of used modality resembles that of the horizontal resolution in DLP-based VPP. On the lateral plane, however, the effective resolution relies heavily on sinogram design and may vary drastically even with the same optics and photoresin formulation. Currently, lateral resolution bottlenecks TVP's achievable precision. Second, the minimum optomechanical requirements to achieve a reported feature size are often missing. Third, is delineating the effects of dose buildup from that of material dependence reasonable? The essential thresholding effect that separates in-part voxels from out-of-part voxels is dependent on photoresin formulation, and the resulting smallest features can be optimized via meticulous trial and error and will be impacted by post-processing before any *ex-situ* characterization. Conversely, TVP has a general upper limit of achievable precision, defined by the imaginary dose buildup in vacuum via back-projection, which is material independent and would be affected by only the optomechanics. Fourth, is the same feature size reproducible in all geometric designs, or there exist design constraints if certain fabrication resolution were to be achieved. Here, to address these concerns, we first show that with illumination of a single color, TVP is not a freeform approach when operating at the optical resolution of the modality. We then prove that introducing polyspectral reconstruction allows a dual color implementation of TVP with the same optomechanical modality to achieve all three key milestones of freeform manufacturing simultaneously.

The Angular Resolution Dilemma

We first introduce an eight-step protocol for sinogram generation (Fig. S1). The protocol guarantees that a minimum number of pixels, N , of arbitrary position and greyvalue, can be fidelously recovered on the lateral plane via back-projection. We then show that N is a measure of design freedom, and limits the lateral resolution of single color TVP.

Sinogram compiles the illuminating intensities for a row of mirrors on a digital micromirror device (DMD) from all projecting angles. Pixels in the original 2D design are to be processed sequentially. For the n -th pixel P_n of arbitrary position and greyvalue I , a sinogram can be generated iteratively in 8 steps (Fig. S2):

- 1- Identify the trajectory of P_n ;
- 2- Calculate light attenuation between P_n and the source of illumination along the trajectory;
- 3- Identify the intersections between P_n 's trajectory and the other $n-1$ trajectories;
- 4- Calculate the accrued dose of illumination (I_c) that P_n had received from these intersections;
- 5- Calculate the dose mismatch $\Delta I = I - I_c$;
- 6- Distribute ΔI over the non-intersecting sections of P_n 's trajectory;
- 7- Calculate the emitting intensity I_0 for delivering ΔI ;
- 8- Move to P_{n+1} .

Here we adopt the parallel beam assumption for simplicity: P_n is only illuminated by one mirror at any instant, whereas each mirror illuminates multiple pixels whose distance to the rotation axis (r) is greater than the distance between the mirror and the center of the DMD aligned with the axis (x) (Fig. S3). To guarantee fidelous recovery of P_n , there must be at least one angle from which ΔI can be supplemented, given $I_0 \in \mathfrak{R}$. During a full rotation, any two continuous trajectories intersect exactly twice, at the two opposite projecting angles at which two pixels shadow each other. If we choose to space all projecting angles evenly by $\Delta\theta$, guaranteeing fidelous reconstruction of $N+1$ points requires that $2\pi/\Delta\theta > 2N$. N is the minimum number of fidelously recoverable pixels if $I_0 \in \mathfrak{R}$. The greater the N is, the more greyscale pixels could be freely placed in a design. However, this freedom cannot be increased indefinitely by reducing $\Delta\theta$, because the DMD has a finite pixel pitch (p). To make stepwise rotation meaningful, $\Delta\theta$ has to be sufficiently large, so that $d \cdot \sin \Delta\theta \geq p$, in which d is the fabrication resolution of TVP, i.e., the smallest distance between two differentiable points. Violating this inequity results in two trajectories intersecting at more than two projecting angles on a discretized sinogram.

Combined, angular resolution $\Delta\theta$ defines a dilemma between fabrication resolution and design freedom for TVP operating at a single wavelength, i.e., $\arcsin(p/d) \leq \Delta\theta \leq \pi/N$. It follows that orthogonal illumination would be required to achieve a fabrication resolution on par with the optical resolution ($\Delta\theta = \pi/2, p = d$). Noteworthy is that N is a measure of design freedom, not the actual number of lossless pixels. There are designs that could be fully recovered even at very low N (e.g., orthogonal line pairs). $I_0 \in \mathfrak{R}$ is practically unachievable for TVP because $I_{0,max}$ is capped by the maximal output of a projector, and $I_{0,min} \neq 0$ because of projectors' non-zero black

luminance. Most importantly, all current TVP modalities are subject to a positivity constraint ($I_0 \in \mathfrak{R}^+$), and cannot cope with $\Delta I < 0$ even in the presence of available projecting angle(s).

Polyspectral Reconstruction

Pseudo-negative illumination (PNI) can be introduced by modulating the illumination of a second wavelength that counteracts the primary wavelength's effect on inducing polymerization. Although the $\Delta\theta$ dilemma applies to each wavelength, the superposition of multiple dose profiles changes the effective dependence of resolution (d) on pixel pitch (p). Here we use a 3×3 dot array to demonstrate the deteriorating effect of increasing design freedom and the improvements enabled by PNI. The array is embedded in binary pixels and is reconstructed using a row of 16 mirrors of the same pitch (Fig. S4). We designate visible light as the primary printing color and ultraviolet (UV) light as the PNI. If the mirrors modulate only visible light, we label the scheme and pertaining results as "single color" (SC). If each mirror modulates either visible or UV light at any instant, we use the label "dual-color mono-spectral" (DC-mono). If each mirror modulates both UV and visible light simultaneously, we use the label "dual-color polyspectral" (DC-poly). A major difference between DC-mono and DC-poly is that the latter creates both positive and pseudo-negative illumination along the same ray by exploiting different extinction factors (Fig.1A). If the intensities of different wavelengths are stored in the RGB channels separately, the sinogram would contain only green pixels for SC, either green or red pixels for DC-mono, and green, red or yellow pixels for DC-poly (Fig.1B).

Although SC-TVP could deliver features on par with the optical resolution when $N=2$, the achievable dose contrast between in-part and neighboring out-of-part voxels requires a delicate control of process termination. The very narrow process window (period in which illumination is

cut off to avoid quality deterioration due to overexposure) may hamper the identification of SC-TVP's achievable precision. Decreasing $\Delta\theta$ drastically increases the distance between differentiable points according to $d \cdot \sin \Delta\theta \geq p$. Superposing two independent dose profiles, however, effectively restrains the dispersion and contains the peak dimensions (Fig.2C). When $N = 2$, both DC schemes fidelously reproduced the array at 50% dose contrast, whereas SC led to overexposure between the square dots (Figs 2B, S4). When $N = 360$, DC-poly reproduced the array with distorted unit shapes, DC-mono was not able to prevent overexposure between the central dot and its 4 nearest neighbors at a 50% contrast, whereas SC could no longer reproduce the array without causing significant overexposure.

Given an optical setup (p) and required fabrication resolution (d), the achievable design freedom is limited by $N < \pi/\arcsin(p/d)$. In practice, a design often contains far more pixels than could be guaranteed by N . It is therefore informative to look at the behaviors of different schemes beyond allowed design freedom. Here we use a 29×29 phantom model ($n = 841$ pixels) to demonstrate the differences. We computed the sinogram for a row of 100 mirrors at $\Delta\theta = 5^\circ$ ($N = 36 \ll n$). We first followed the eight-step protocol to find out the number of fidelously reconstructed pixels. As the processing progresses, fidelous reconstruction may no longer be possible, due to either the positivity constraint or the absence of projecting angle. In the former, we proceeded by reducing the doses imbued at existing intersections. In the latter, we distributed ΔI evenly over the entire trajectory. For DC-mono, there is only one sinogram and thus one trajectory. For DC-poly, the sinograms are separated: when $\Delta I > 0$, only the sinogram for visible light is updated, and when $\Delta I < 0$, only the sinogram for UV light is updated (Fig. S1). We then evaluated the change in overall fidelity loss, calculated as the Frobenius norm of the difference

between design and dose profile. We only accepted changes to the intersections when the compromise to the fidelity of processed pixels is outweighed by the contribution to the global fidelity of adding the new pixel. A pixel triggering such an event is counted as *compromised*. When it is impossible to find a globally favored update to an existing sinogram, the pixel was dropped and labelled as *missed*. For the phantom model, polyspectral reconstruction outperformed its counterparts with the fewest missed pixels (Fig.1C) and less fidelity compromise at the intersections compared to DC-mono (Fig. 1D).

Stability Control for Greyscale Printing

One can realize PNI by using binary photoinhibition (BPI) to moderate the induction period stemming from a pre-dissolved radical quencher A (e.g., oxygen). We look for a chemical species B that meets four requirements:

1. Competes with A for incident dose of primary illumination (e.g., visible light)
2. Generates upon the illumination of a secondary color (e.g., UV light)
3. Is stable in the absence of the secondary illumination
4. Quenches free radicals

With B, the nonlinearity that separates in-part from out-of-part voxels in a single-color implementation of TVP will be replaced by a dynamic, illumination-driven system that enables greyscale printing. The skeleton reactions of BPI and the corresponding rate laws are:





r_i indicates the rate of elementary reaction i , square brackets indicate concentration (M), t is time (s), k_A , k_B , k_C are zeroth-order rate constants ($\text{Ms}^{-1}\text{W}^{-1}$), k_2 is second-order rate constant ($\text{M}^{-1}\text{s}^{-1}$), I_{vis} and I_{UV} , are irradiance of visible and UV light (W), respectively. The stability of B in the absence of UV is defined by r_4 . The system is governed by

$$\frac{d[A]}{dt} = -k_A I_{vis} \frac{[A]}{[A] + [B]} = F_1, \quad (5)$$

$$\frac{d[B]}{dt} = -k_B I_{vis} \frac{[B]}{[A] + [B]} + 2k_C I_{UV} - 2k_2 [B]^2 = F_2, \text{ and} \quad (6)$$

$$\frac{d[C]}{dt} = -k_C I_{UV} + k_2 [B]^2 = F_3 \quad (7)$$

On the phase diagram, only the origin represents the depletion of all quenchers and thus the initiation of polymerization (Fig. 3A). The trajectory of any point in the curing volume can be steered via manipulating the irradiance (I_{vis} and I_{UV}). When a system revolves counterclockwise around the origin, i.e., $[A] \cdot F_1 + [B] \cdot F_2 = 0$, the co-illumination brings the system neither closer nor farther away from polymerization, and thus effectively cancel out each other, i.e., UV

becomes the PNI of visible light, and vice versa. The system has a single stationary state (SS)

$\left(0, \sqrt{\frac{2k_C I_{UV} - k_B I_{Vis}}{2k_2}}\right)$, the stability of which is given by the linearization in its neighborhood:

$$\begin{bmatrix} \frac{\partial F_1}{\partial [A]} & \frac{\partial F_1}{\partial [B]} \\ \frac{\partial F_2}{\partial [A]} & \frac{\partial F_2}{\partial [B]} \end{bmatrix}_{SS} = \begin{bmatrix} -k_A I_{Vis} \sqrt{\frac{2k_2}{2k_C I_{UV} - k_B I_{Vis}}} & 0 \\ k_B I_{Vis} \sqrt{\frac{2k_2}{2k_C I_{UV} - k_B I_{Vis}}} & -2\sqrt{2k_2(2k_C I_{UV} - k_B I_{Vis})} \end{bmatrix}, \quad (8)$$

with eigenvalues

$$\lambda_1 \cdot \lambda_2 = 4k_2 k_A I_{Vis}, \text{ and} \quad (9)$$

$$\lambda_1 + \lambda_2 = -k_A I_{Vis} \sqrt{\frac{2k_2}{2k_C I_{UV} - k_B I_{Vis}}} - 2\sqrt{2k_2(2k_C I_{UV} - k_B I_{Vis})}. \quad (10)$$

The signs suggest that both the position and the stability of the SS are governed by dual color incidence. Changing I_{vis} and I_{UV} may swap the SS between being stable and being an oscillatory center (Fig. 3B-C, Movie S1). In addition to delivering negativities, the controllable stability enables the pinning of out-of-part voxels to the upper y-axis, prolonging the process window. Voxel-level delayed initiation of polymerization also enables greyscale printing with significantly improved orthogonality between geometry and mechanical property modulation.

Exemplary Photochemical Implementation

Inspired by T. Scott's group's work (8-10), we evaluated the suitability of tetraethylthiuram disulfide, butyl nitrite and 2,2'-Bis(2chlorophenyl)-4,4',5,5'-tetraphenyl-1,2'-biimidazole (*o*-Cl-HABI) as sources of B. Here we use *o*-Cl-HABI as an example because of its relative stability

and optical property (Figs S8-16, S26). At selected concentrations, the extinction coefficient of the formulated photoresin allowed both visible and UV light to penetrate through the entire curing volume. Photolysis upon UV illumination cleaves an *o*-Cl-HABI molecule into two lophyl radicals, which quenches free radicals generated upon visible illumination in a way that effectively resembles what oxygen does in the TVP context. The self-recombinatorial reaction of lophyl radicals features a half-life comparable to the time of a typical TVP process and is thus less energetically demanding for the UV irradiance. Although lophyl radical is not an ideal species B because of *i*) its limited lifespan, *ii*) the low storage capacity of diluted *o*-Cl-HABI and *iii*) the coloration upon photolysis, the resin formula nonetheless synergized with DC-TVP to deliver remarkable improvements in quality compared to its SC counterpart.

Fig. 4A-K shows the anticipated improvements in design freedom. The modulation transfer function (MTF) of fabrication in Fig. 4F is determined as $(\overline{I}_i - \overline{I}_o) / (\overline{I}_i + \overline{I}_o)$, in which \overline{I}_i and \overline{I}_o are averaged dose buildup for in-part and out-of-part voxels, respectively. This is the theoretical MTF given an ideal optical modality. The experiments were carried out using a commercial projector with an optical MTF of 0.64 when operating at $p = 15 \mu\text{m}$. At low design freedom ($N = 2$), SC-TVP could achieve precision on par with the optical resolution. When $N = 360$, however, features get smeared out (Fig. 4H) and the fabrication MTF deteriorates drastically with increasing dots per inch (DPI) of the design. With PNI, the DC-poly scheme delivered superior quality at a low N by preventing overexposure between line intersections (Fig. 4A-C vs. G-I). At high N , DC-TVP maintains the achievable MTF near unity even when operating near the optical resolution. To minimize the uncertainties introduced during post-processing, we relied primarily on *in situ* shadowgraphy and resorted to *ex situ* characterization only when the achieved

fabrication resolution exceeded the resolving capacity of the lateral imaging modality. For SC-TVP, we were not able to capture features beyond a design DPI of 676 when operating at $N = 360$ (Fig. 4K), and the observed feature size was $81\ \mu\text{m}$ (Table S3). For DC-TVP operating at $N = 360$, we captured highly reproducible features at the pitch of camera pixel ($27\ \mu\text{m}$) with the same imaging modality when design DPI = 1016, corresponding to design features of $25\ \mu\text{m}$ (Fig. 4D). We also confirmed with optical microscopy that the DC-poly scheme delivered features at the optical resolution of the projecting modality ($15\ \mu\text{m}$) when operating at $N = 2$ (Fig. 4E). Overall, polyspectral reconstruction increases the design freedom by at least two orders of magnitude (measured by N) without significant compromise of MTF, thus achieving freedom of design at a precision on par with the specification of the optomechanical modality.

In the lateral plane where features were produced via tomographic reconstruction, the DC-poly scheme managed to recover very fine details in complex geometries (Fig. 4L-S). Similar levels of fidelity appeared to be unattainable by our team using the SC scheme with the same modality, however optimizations were carried out. The designs were all binary images of 1500×1500 pixels, and were printed in $\text{Ø}30$ mm vials (Movies S2-5). Stacking images like these, DC-TVP allows a typical multiwavelength 4K light engine to deliver workpieces containing up to 8.9 billion voxels ($1520 \times 1520 \times 3840$) in a $\text{Ø}30 \times 50\ \text{mm}^3$ curing volume in a few minutes at two-digit-micrometer fabrication resolution. We observed in virtually all cases qualitative improvements compared to our previous SC and DC-mono works (Fig. 4T-X, Movies S6-8). Fig. 4T shows a 45-floor “twisted torso” with 400 cubic compartments on each floor, printed in 6 minutes. Fig. 4W shows an orthogonal lattice built in 150 seconds. It was comparably easier to

maintain the internal hollowness of these architectures using the DC-poly scheme (Movie S6 and Fig. 4X) than the SC scheme, although post-processing still poses significant challenges.

Polyspectral reconstruction also offers prolonged process window and enables greyscale printing. Figs 4R-S show snapshots taken 120 seconds apart at under- and over-exposed status. With the SC scheme, the overexposure in-between the features was evident. Greyscale printing was showcased using a pie chart containing six distinct intensity grades (Figs 4Y-Z). With the SC scheme, achieving graded internal property while maintaining the overall geometric fidelity was challenging due to the mismatch between the process window and the time needed to fully establish internal contrast. A compromise to the overall geometry had to be made with the SC scheme, whereas DC-TVP was not subject to such conundrum. The moduli extracted from texture analyzer (Fig. S27) also suggested that DC-TVP realized greyscale property modulation while delivering significantly greater macroscopic fidelity.

Discussion

In TVP, we consider it imperative to recognize the fundamental difference between the lateral plane and the axial direction when reporting fabrication resolution. The sizes of smallest features found in the literature could differ for various geometric designs, projector setups, resin formulations, angular resolutions and for lateral and vertical planes. We argue that lateral resolution is the bottleneck of TVP's precision, and should be reported in direct connection with both optical resolution and the allowed design freedom. We showed that DC-TVP delivers modality-level precision with high design freedom at an inherent dimensionality of three – reaching the three key milestones for freeform manufacturing simultaneously. The experimental results are expected to be further improvable directly upon modality upgrades.

We note that the absence of a well-established post-processing protocol poses an imminent obstacle to the popularization of TVP. In this study, the success rate of handling large workpieces with delicate, sub-millimeter features was modest even with the most well-trained specialists. While producing better internal hollowness, the preservation of structural integrity tends to be more challenging with BPI, because species B arrests the extent of polymerization. Worth mentioning is that introducing PNI enables the direct transfer of knowledge on improving CT reconstruction to optimize TVP quality. For example, Ram-Lak filtering can now be applied directly to a sinogram, producing illuminating patterns for the mono-spectral scheme.

Lophyl radicals generated from *o*-Cl-HABI could be replaced by a more suited candidate that has a greater storage capacity ratio while being indefinitely stable without secondary illumination. Movies S9-11 visualize the differences between our exemplary chemical implementation and a single-color system using reactive-transport simulations. We envision that deploying an ideal BPI reagent will avoid the need of pre-dissolved quencher because dose contrast can be created effectively *in situ*, further increasing fabrication speed by shortening or even eliminating the induction. Although we focused on a dual-color system, the methodology could be extended to systems responsive to three or more spectral regions (*II*), turning TVP into an integrated approach of both additive and subtractive manufacturing.

References and Notes

1. V. Fleury, J.-F. Gouyet, M. Léonetti, *Branching in nature: Dynamics and morphogenesis of branching structures, from cell to river networks*. (Springer Science & Business Media, 2013), vol. 14.
2. E. C. Novosel, C. Kleinhans, P. J. Kluger, Vascularization is the key challenge in tissue engineering. *Adv Drug Deliv Rev* **63**, 300-311 (2011).
3. B. E. Kelly, I. Bhattacharya, H. Heidari, M. Shusteff, C. M. Spadaccini, H. K. Taylor, Volumetric additive manufacturing via tomographic reconstruction. *Science* **363**, 1075-1079 (2019).
4. D. Loterie, P. Delrot, C. Moser, High-resolution tomographic volumetric additive manufacturing. *Nat Commun* **11**, 852 (2020).
5. B. Wang, E. Engay, P. R. Stubbe, S. Z. Moghaddam, E. Thormann, K. Almdal, A. Islam, Y. Yang, Stiffness control in dual color tomographic volumetric 3d printing. *Nat Commun* **13**, 367 (2022).
6. J. Madrid-Wolff, J. Toombs, R. Rizzo, P. N. Bernal, D. Porcincula, R. Walton, B. Wang, F. Kotz-Helmer, Y. Yang, D. Kaplan, Y. S. Zhang, M. Zenobi-Wong, R. R. McLeod, B. Rapp, J. Schwartz, M. Shusteff, H. Talyor, R. Levato, C. Moser, A review of materials used in tomographic volumetric additive manufacturing. *MRS Communications*, (2023).
7. Q. Thijssen, J. Toombs, C. C. Li, H. Taylor, S. Van Vlierberghe, From pixels to voxels: A mechanistic perspective on volumetric 3d-printing. *Progress in Polymer Science*, 101755 (2023).
8. T. F. Scott, B. A. Kowalski, A. C. Sullivan, C. N. Bowman, R. R. McLeod, Two-color single-photon photoinitiation and photoinhibition for subdiffraction photolithography. *Science* **324**, 913-917 (2009).
9. H. L. van der Laan, M. A. Burns, T. F. Scott, Volumetric photopolymerization confinement through dual-wavelength photoinitiation and photoinhibition. *ACS Macro Lett.* **8**, 899-904 (2019).
10. M. P. de Beer, H. L. van der Laan, M. A. Cole, R. J. Whelan, M. A. Burns, T. F. Scott, Rapid, continuous additive manufacturing by volumetric polymerization inhibition patterning. *Sci Adv* **5**, eaau8723 (2019).
11. T. L. Rapp, C. A. DeForest, Tricolor visible wavelength-selective photodegradable hydrogel biomaterials. *Nature Communications* **14**, 5250 (2023).

Acknowledgments: We thank Mark Smith and 3Shape A/S for providing the E-series laboratory scanner; Christof Hieger, Arturo Bianchetti, Ecem Badruk and IN-VISION Technologies for providing the TwoWave projecting modality; Esben Thormann for access to optical microscopy; Josefine F. Lønholdt, Jane Pedersen, Yan Wei, Stefan Bruns and Christina Schmidleithner for helpful discussions and resource acquisition; Mariusz Kubus for assistance in FTIR measurement; Peter R. Stubbe for guidance in mechanical testing; Ishaq Khaliqdad and Andreas G. Pedersen for TVP prototyping; Christina B. Nielsen for assistance in chemical analysis and management. We are grateful to the 3D Imaging Center at the Technical University of Denmark for providing access to X-ray computed tomography equipment and the Thingiverse community for creating high quality STL files for 3D printing research.

Funding:

Villum Foundation grant 40805 (YY)

Independent Research Fund Denmark grants 0136-00043 and 8022-00162 (YY)

Innovation Fund Denmark InnoExplorer (YY)

DTU Skylab Discovery Grants and Proof of Concept Grants (YY)

China Scholarship Council grant 202006130009 (BW, AI)

Author contributions:

Conceptualization: YY

Methodology: BW, HSM, JRF, YY

Investigation – experimental: BW, WS, JPCN, HSM, TDVC, AAS

Investigation – modelling: YY

Funding acquisition: KA, AI, YY

Project administration: YY

Supervision: JRF, HOS, KA, AI, YY

Writing – original draft: BW, YY

Writing – review & editing: All authors

Competing interests: YY declares that a patent has been filed related to the topic covered in this publication. WS is an employee of PERFI Technologies ApS. YY is the chief scientific advisor to PERFI Technologies ApS. The remaining authors declare no competing interests.

Data and materials availability: All data analyzed in this manuscript are included in the main text or the supplementary materials.

Supplementary Materials

Materials and Methods

Supplementary Text

Figs S1 to S28

Tables S1 to S3

Movies S1 to S11

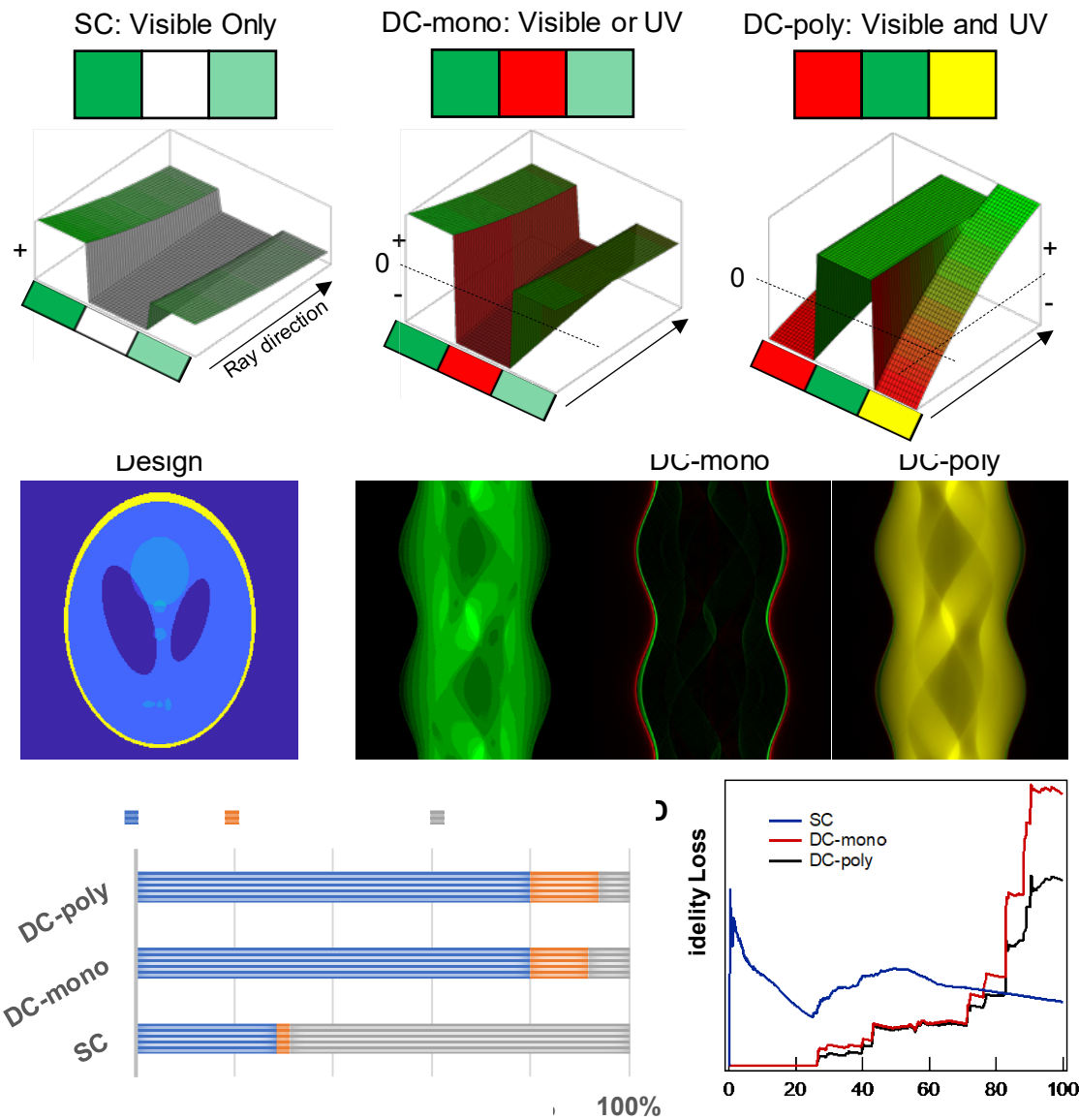


Fig. 1. TVP illumination schemes. (A) Contrast building mechanisms. SC: single-color scheme, in which only one wavelength is used to initiate polymerization. Dose contrast is created by cumulating positive intensity differences between rays. DC-mono: dual-color, mono-spectral scheme, in which dose contrast can be enhanced between rays of different wavelengths that effectively negate each other. DC-poly: dual-color, polyspectral scheme. The same mirror on a digital micromirror device (DMD) is used to modulate rays of more than one wavelength. The

difference between the extinction factors creates an effectively increasing dose profile (instead of attenuating) in the propagating direction. Dose contrast can be enhanced both between rays and along the same ray. **(B)** Exemplary sinograms for the phantom model when stored in the RGB format. The SC scheme contains only green pixels representing intensities of visible light illumination. DC-mono contains either green or red pixels, the latter representing intensities of UV light illumination. DC-poly contains both green, red and yellow pixels. **(C-D)** Fidelity loss in various schemes when a phantom model is processed following the eight-step protocol (Fig. S1). The primary loss stems from the missed pixels. The secondary loss in (D) corresponds to the undesirable greyvalue changes in the compromised pixels only, and does not reflect the loss due to missed pixels.

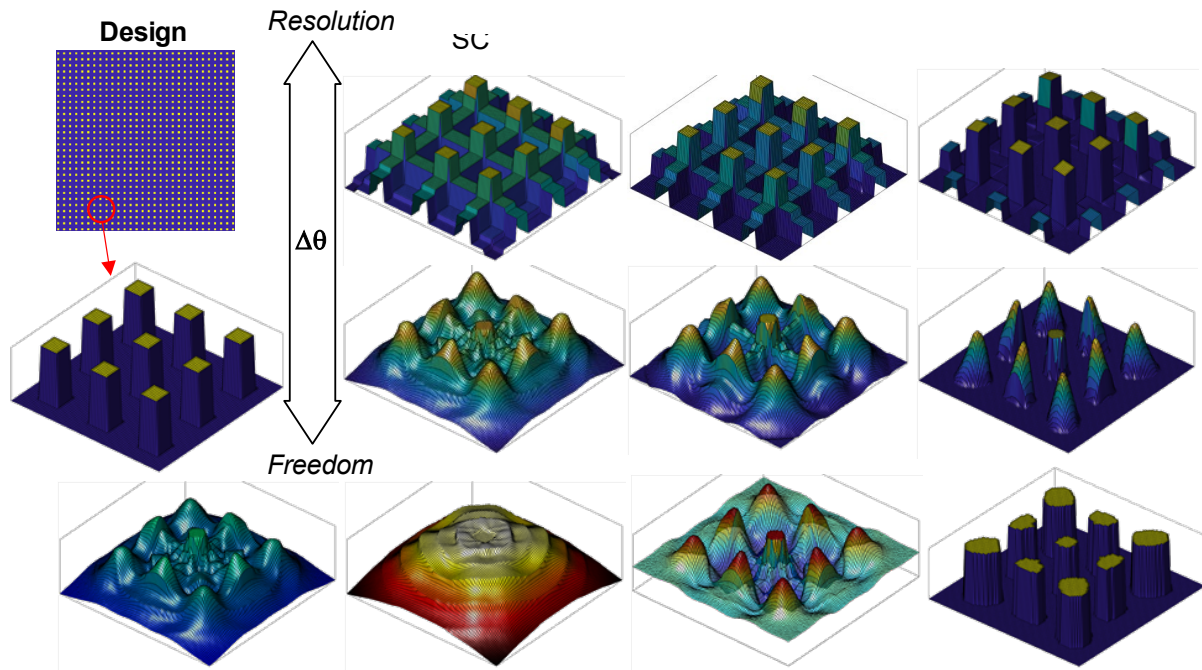


Fig. 2. Impact of design freedom on achievable fabrication resolution. (A) The binary design with ones periodically embedded in zeros on the lateral plane. (B) The angular resolution dilemma manifested in different illumination schemes. The total number of projecting angles (N), which increases inversely with angular resolution $\Delta\theta$, is a direct measure of design freedom. In the SC scheme, features on par with the pixel pitch of the projecting modality can only be achieved with orthogonal illumination ($\Delta\theta = 90^\circ$). Refining angular resolution to 0.5° smears out the built-up, resulting in greater feature sizes upon thresholding. This dilemma does not apply to the DC schemes, and the DC-poly scheme offers the most significant improvement in fabrication resolution with high design freedom. (C) Superposition of DC-poly dose profiles. The imaginary dose built-ups for visible and UV light in vacuum can be superposed via devised photochemistry to produce small features at very fine angular resolution.

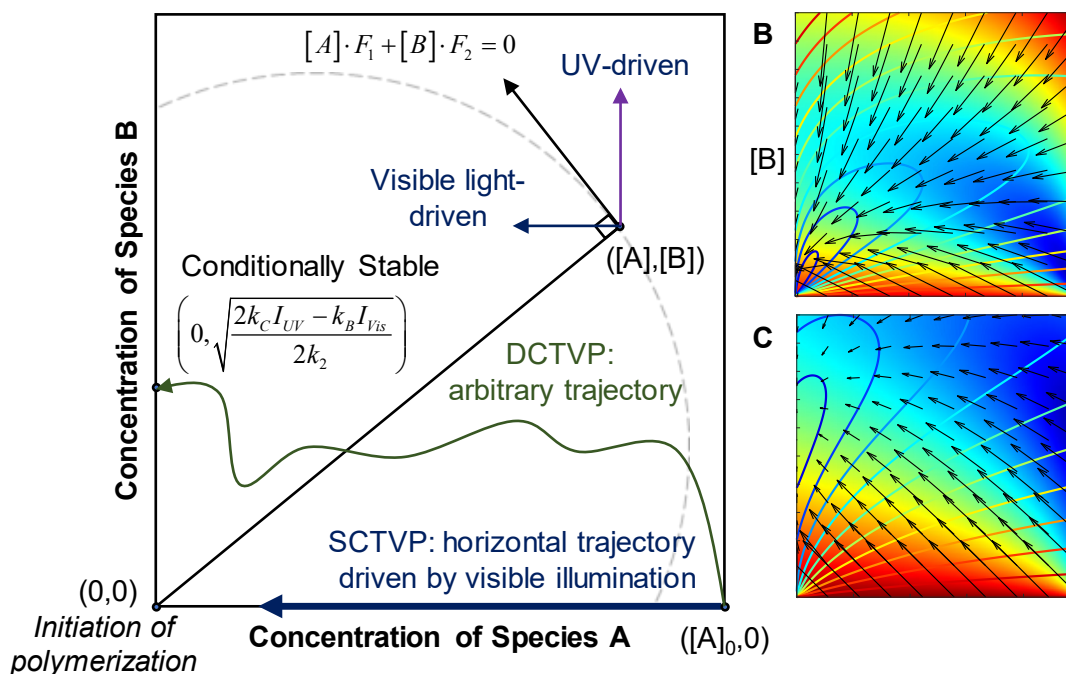


Fig. 3. Phase diagram for binary photoinhibition. (A) Pseudo-negative illumination is created when the co-illumination of two wavelengths steer a system to revolve counterclockwise around the origin ($[A] \cdot F_1 + [B] \cdot F_2 = 0$), the latter being the only state triggering polymerization.

Coordinating the irradiance of visible and UV light enables both free design of system trajectory for each and every point in the curing volume individually, and the creation of stable stationary states that will not trigger polymerization in the upper y-axis. (B-C) Exemplary phase diagrams for in-part (B) and out-of-part (C) voxels. See Movies S1, S8-10 for system dynamics during a typical TVP process.

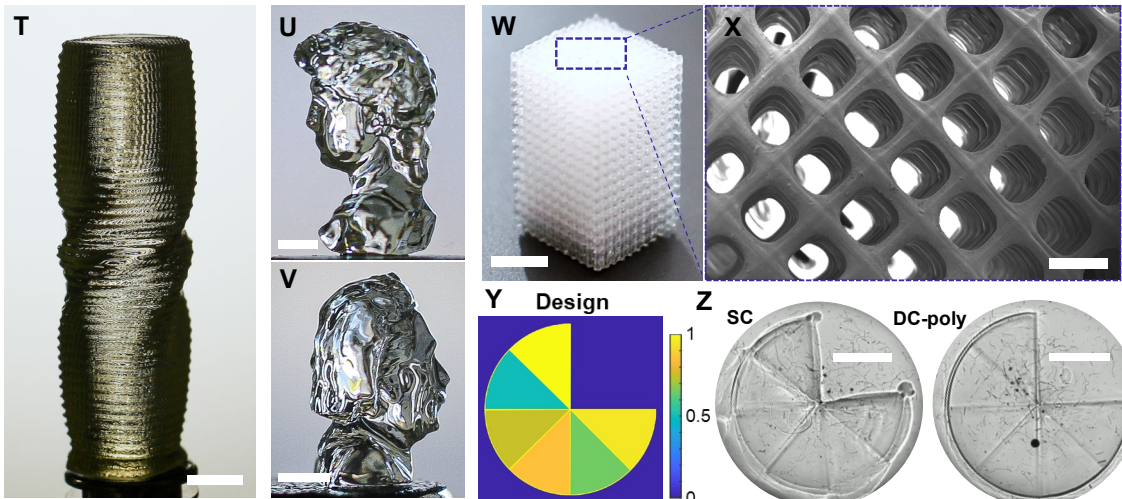
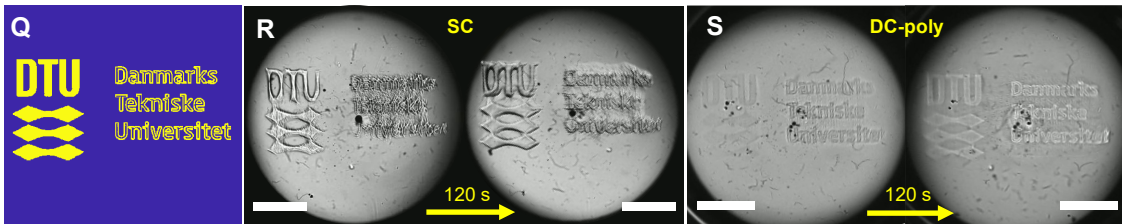
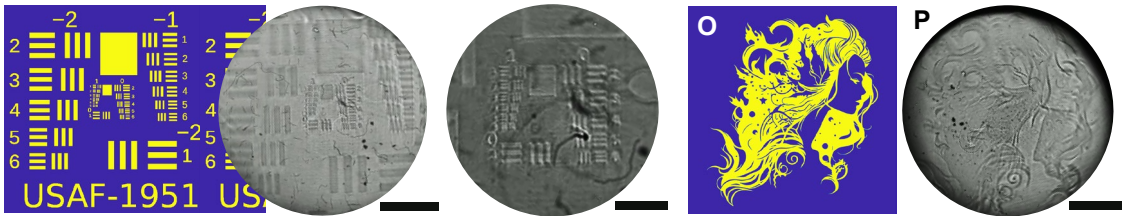
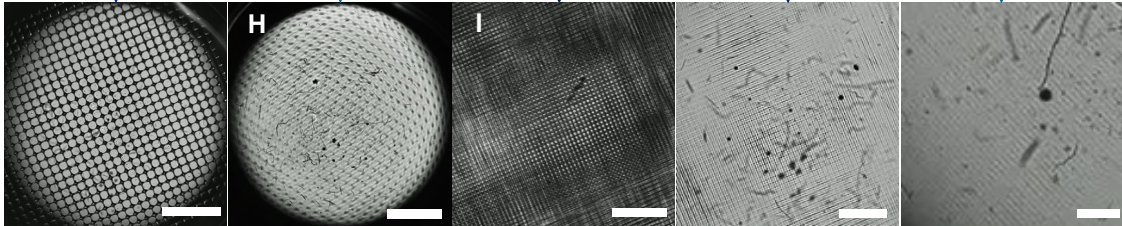
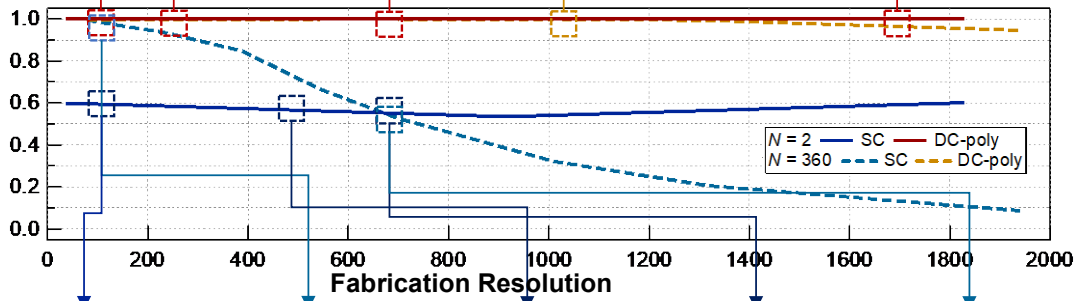
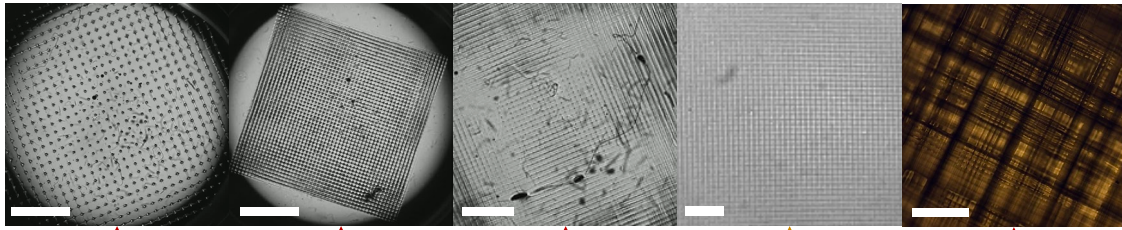


Fig. 4. Improvements in design freedom and fabrication resolution enabled by polyspectral reconstruction. (A-E) Fabrication resolution of the DC-poly scheme at various design DPI (dots-per-inch). The experiments were carried out using a commercial 4K projecting modality with pixel pitch of 15 μm operating at modulation transfer function (MTF) of 0.64. The periodical features observed with *in situ* shadowgraphy were 243 μm , 162 μm , 54 μm and 27 μm in (A-D). Features on par with the optical resolution (15 μm) was observed using optical microscopy in (E). (F) Theoretical fabrication MTF of DC-poly vs. SC schemes for an ideal projecting modality operating at optical MTF = 1. The fabrication MTF is calculated using the average doses in in-part and in out-of-part voxels after back-projecting sinograms to create an imaginary dose profile in vacuum without thresholding, as seen in Fig. 2B. (G-K) Fabrication resolution of the SC scheme at various design DPI. The smallest differentiable features were observed when design DPI = 676. From G to K, the features were 243 μm , 243 μm , 108 μm , 81 μm and 81 μm in size. No finer feature was observable for $N = 360$ with the SC scheme using *in situ* shadowgraphy. (L-N) A 1500 \times 1500 US Air Force resolution target printed laterally in its entirety in a $\text{\O}30$ mm vial. (N) is a zoom-in of the same workpiece in (M) showing the smallest target set at the center. See also Movie S2. (O-P) A 1500 \times 1500 artistic design printed laterally in a $\text{\O}30$ mm vial in 6 minutes. See also Movie S3. (Q-S) Lateral printing of a 1500 \times 1500 DTU logo using the SC (R) and DC-poly (S) schemes. The snapshots were taken 120 seconds apart at an under- and an over-exposed stage of the process. See Movies S9-11 for reactive transport simulations tracking the transition between these stages for a simpler design. (T) A 45-floor “twisted torso” containing 400 cubic compartments per floor, printed in a $\text{\O}30\times 50$ mm vial in 6 minutes. The internal hollowness upon completion can be observed in Movie S6. (U-V) 3D workpieces: busts of David (Movie S7) and Albert Einstein (Movie S8). See also Fig. S4 for

more workpieces. **(W-X)** 10×10×20 lattice printed in 150 seconds. All compartments were clearly patent and can be seen through. **(Y-Z)** Greyscale printing. Both schemes realized property modulation via creating internal dose contrast, while the DC-poly scheme produced significantly greater geometric fidelity. See all six moduli extracted using a texture analyzer in Fig. S27. (Resin formula: 2M-0.4, see Table S1; Scalebars A-B: 5 mm, C: 2 mm, D-E: 500 μm, G-H: 5 mm, I-J: 2 mm, K: 500 μm, M: 5 mm, N: 2 mm, P: 5 mm, R-S: 5 mm, T: 5 mm, U-V: 2 mm, W: 3 mm, X: 500 μm, Z: 5 mm)

Materials and Methods

Materials

The methacrylate based photoresin was prepared by mixing triethylene glycol dimethacrylate (TEGDMA, CAS#109-16-0, Sigma–Aldrich) and bisphenol A glycerolate dimethacrylate (bisGMA, CAS#1565-94-2, Sigma–Aldrich) at a weight ratio of 1:1 or 2:1. Camphorquinone (CQ, CAS# 10373-78-1, $\geq 96.5\%$ purity, Sigma–Aldrich) and ethyl 4-dimethylaminobenzoate (EDAB, CAS# 10287-53-3, Sigma–Aldrich) were added as the photoinitiator and co-initiator, respectively. 2,2'-Bis(2chlorophenyl)-4,4',5,5'-tetraphenyl-1,2'-biimidazole (*o*-Cl-HABI, CAS# 7189-82-4, TCI Europe) was first dissolved in tetrahydrofuran (THF, CAS# 109-99-9, Fisher Scientific) at 28 wt% then added to the photoresins.

An alternative acrylate based resin was prepared by mixing bisphenol A glycerolate diacrylate (BPAGDA, CAS# 4687-94-9) and poly(ethylene glycol) diacrylate (PEGDA, CAS# 26570-48-9, average Mn 250 w/100 ppm 4-methoxyphenol as inhibitor) in the weight ratio of 1:1 or 2:1, incorporating CQ and EDAB as the initiator and co-initiator respectively. *o*-Cl-HABI solution (28 wt% *o*-Cl-HABI: 72 wt% THF) was then added to the mixture at varied weight ratios. 2,2,6,6-Tetramethylpiperidine 1-oxyl (TEMPO, CAS# 2564-83-2, Sigma–Aldrich) was incorporated as extra inhibitor. All the chemicals were obtained and used as received without further purification. All the resin formulations are listed in Table S1.

Table S1. Resin formulations.

Resin name	Monomer (weight ratio)	CQ	EDAB	<i>o</i> -Cl-HABI	TEMPO
M-0.5	bisGMA/ TEGDMA (1:1)	0.2 wt%	0.5 wt%	0.5 wt%	0
M-1	bisGMA/ TEGDMA (1:1)	0.2 wt%	0.5 wt%	1 wt%	0
M-3	bisGMA/ TEGDMA (1:1)	0.2 wt%	0.5 wt%	3 wt%	0
2M-0.4	bisGMA/ TEGDMA (2:1)	0.1 wt%	0.25 wt%	0.4 wt%	0
A250	BPAGDA/PEGDA (1:1)	0.1 wt%	0.25 wt%	0	0
2A250	BPAGDA/PEGDA (2:1)	0.1 wt%	0.25 wt%	0	0
A250-T1	BPAGDA/PEGDA (1:1)	0.1 wt%	0.25 wt%	0	0.29 mM
A250-T2	BPAGDA/PEGDA (1:1)	0.1 wt%	0.25 wt%	0	0.72 mM
A250-0.5	BPAGDA/PEGDA (1:1)	0.1 wt%	0.25 wt%	0.5 wt%	0
A250-1	BPAGDA/PEGDA (1:1)	0.1 wt%	0.25 wt%	1 wt%	0
A250-3	BPAGDA/PEGDA (1:1)	0.1 wt%	0.25 wt%	3 wt%	0

Optomechanical modality

The dual-color tomographic volumetric printing modality is illustrated in Fig. S5, with assembling parts tabulated in Table S2. Component S1 is a dual-color 4K resolution DLP projector (TVP07-15-460/385, Xiamen Zhisen, China), capable of modulating both blue light (460 nm) and UV light (385 nm) in parallel. It is used with a bi-telecentric lens (L1, Xiamen Zhisen, China) to achieve parallel beam relay into the curing volume. The lens system compensates for the achromatic aberration of the two wavelengths. Irradiance was measured as a function of greyscale intensity for both wavelengths (Fig. S7).

Two *in situ* imaging modalities were integrated in the setup. The axial imaging system was illuminated by an LED source (S2, $\lambda = 625$ nm, M625L4-C4, Thorlabs) through a beam expander (BE, D series 5x, Wuhan Baixin, China) to ensure collimated light covers the entire curing volume. A telecentric lens (TL2, ESCM014-180X23, ES technology, China) was used to demagnify the curing volume to the imaging size of the detector (C1, CMOS camera, GS3-U3-51S5M-C, FLIR Grasshopper). The lateral imaging system used a collimated light source (S3) that could directly illuminate the curing volume in the lateral direction, followed by a 4f lens system composed of lens L1 (200 mm, LA1979-N-BK7, Thorlabs) and L2 with an adjustable working distance (25 mm, TECHSPEC59-871, Edmund) to relay the beam to camera C2 (same as C1). The maximal projection area in the focal plane was 34.6 by 61.4 mm², with an effective pixel size of ~ 15 μm . A flat-bottom cylindrical test tube (\varnothing 30 mm) containing photoresin was mounted on a motorized rotation stage. A cuboid vat containing index-matching fluid was placed outside the test tube, with walls perpendicular to incident beams. During printing, the motor and projection were coordinated to avoid fan-shaped voxel formation.

An alternative dual-color setup (365 nm + 460 nm) was also tested. This printer featured a dual-wavelength printer (TWO WAVE LE, Invision, Austria) paired with the built-in lens group (Sphinx). A group of extra lenses was introduced to narrow down the dimensions of the projection plane to 13.1 by 21 mm², with an effective pixel size of 8.2 μm . We also designed a single-color modality consisting of a visible light projector (BenQ LK954ST, BenQ, Sweden) and a doublet achromatic lens (AC508-075-A, Thorlabs), resulting in a 30 by 30 mm² projection field and an effective pixel size of 24 μm .

Optical specifications

We used a modulation transfer function (MTF) to quantify the capability of our optical system to preserve the details of an input image. For the projecting modality, this is defined by

$$MTF = \frac{m_{output}}{m_{input}}, \quad (S1)$$

where m is the intensity contrast of an image

$$m = \frac{I_{max} - I_{min}}{I_{max} + I_{min}}, \quad (S2)$$

and I_{max} and I_{min} are the maximum and minimum light intensity values of a contrast line pair. In this study, the MTF was measured using the slanted-edge method. A slanted-edge image was projected by the projector, and a CMOS camera (CMOS camera, GS3-U3-51S5M-C, FLIR Grasshopper) recorded the output image at the focal plane. The pixel size of the camera was 3.45 μm . Subsequently, the captured images were processed using ImageJ to obtain the MTF values,

utilizing the SE_MTF_2xNyquist plugin. The MTF calculation for the lateral imaging system was adapted from the slanted-edge method. A checkerboard calibration target was placed in the focal plane, and the captured image from detector C2 was then employed for extracting the MTF using ImageJ. Fig. S6. depicts the MTF of the Xiamen Zhisen projecting modality and the lateral imaging system.

Fourier transform infrared spectroscopy

Attenuated total reflectance - Fourier transform infrared spectroscopy (ATR-FTIR) was used to measure double bond conversion (Spectrum 100, PerkinElmer, UK). A 1.5 mm ring was used as sample holder, placed next to the ATR cell of the spectrophotometer. A pipette was used to control the sample volume and transfer the test subjects. The spectra were obtained from 4000 cm^{-1} to 650 cm^{-1} with one scan per 8.3 or 4.3 seconds. Real time conversion was calculated by monitoring the C=C alkene stretch peak at 1638 cm^{-1} and that of the aromatic ring at 1610 cm^{-1} .

During *in situ* measurements, a sample was illuminated using 470 nm blue LED (SOLIS-470C, Thorlabs) and/or 365 nm UV light (M365LP1-C1, Thorlabs). The output power of the LEDs was set via LED drivers, and irradiance was measured prior to each experiment using a standard photodiode power sensor (S120VC, Thorlabs) working in the 200 - 1100 nm wavelength range and recorded with an optical power console (PM400, Thorlabs).

UV-Vis spectroscopy

UV-Vis spectroscopy was performed with an Agilent Instrument Exchanges Service Model G1103A using a 10 mm path length quartz cuvette to measure the absorption character of the chemical reagents. *o*-Cl-HABI and CQ were dissolved in THF and diethylene glycol dimethyl ether (DGDE, CAS# 111-96-6), respectively, at varied concentrations (Figs S8-10). The absorbance spectra were collected from 200 nm to 900 nm. As a reference, the absorption characteristics of the solvents were also measured. The extinction coefficient \mathcal{E} of the reagents was calculated using the Beer-Lambert law

$$A = -\log_{10} \frac{I_t}{I_0} = \varepsilon \ell c, \quad (\text{S3})$$

of which,

ε – extinction coefficient (L/cm/g or L/cm/mol)

ℓ – cuvette path length (10 mm)

c – reagent concentration (g/L or mol/L)

In situ UV-Vis measurement was used to evaluate the evolution of the lophyl radical concentration upon the photolysis of *o*-Cl-HABI. Resin M-1 and 10 mm path disposable cuvettes were used. In each test, UV and visible sources were placed on the opposite sides of the cuvette. In order to remove pre-dissolved oxygen molecules, each sample was first illuminated by visible light for 15 s at 5 mW/cm^2 , then by UV for 20 s (Fig. S26). The *in situ* absorbance was recorded every 6.9 s. All measurements were carried out in a dark environment.

Mechanical characterization

Compressive tests were conducted using a Texture Analyzer (Stable Micro Systems, Godalming, UK). A cylindrical metal probe ($\varnothing 2\text{ mm}$) was used with an advancing speed of 0.1

mm/s. The compressive stress was recorded as a function of strain, from which the corresponding elastic modulus was extracted.

Post processing

Isopropanol was used to rinse off residual resin attached to the workpiece after printing. Additional postprocessing, when sample hardening was needed (not in greyscale printing), was conducted by placing a sample in an inner gas (nitrogen or argon) environment and exposing it to 470 nm blue LED light (SOLIS-470C, Thorlabs) for 30 minutes.

Other characterization methods

Scanning electron microscope (SEM) imaging was carried out using an AFEG 250 Analytical ESEM (Oxford instruments). The sample was coated with a 5 nm thick layer of gold using a Quorum coater (Q150T es) before each analysis. Optical microscopy was conducted using Nikon eclipse LV100ND optical microscope with a 5× magnification lens.

Sinogram computation

The eight-step protocol is visualized in Fig. S1. and elaborated in the main text. Sinograms of the DC-mono scheme were generated by applying the Ram-Lak filter to forward projection. The SC and DC-poly schemes used the iterative dose matching algorithm previously developed in our group (5). An STL file was sliced using ChiTuBox (CBD-Tech, SZX) and the grey values of the pixels in the resulting TIFF stack were adjusted in accordance with desired target dose distribution. The initial sinogram was computed using naïve forward projection, i.e. for each projecting angle θ , the position $D(d)$ of the projection of point P(x,y) on a 1D detector was determined by $d = y \cos \theta - x \sin \theta$ and the grey value of P was added to the light intensity at D . The initial sinogram thus generated was back-projected to estimate reconstruction quality. We used a logistic equation to simulate the nonlinear response of free radical polymerization to energy build-up. The workpiece was then compared with the original design and the difference was forward projected to generate a correction for the previous sinogram. The correction may result in negativities, which will impact the quality of reconstruction (Fig. S18). In the SC scheme negativity removal prevented the sinogram from fully reconstructing the desired geometry, and thus the heuristic thresholding became essential in generating sinograms for satisfactory print quality.

Numerical simulation

Simulation of printing process follows our previous numerical scheme (5). The curing volume was discretized using the same voxelization scheme in sinogram computation and the reactive transport of oxygen (A), lophyl radical (B) and *o*-Cl-HABI (C) was analyzed by solving

$$\frac{dc}{dt} = \nabla^2 c + Da \quad (S4)$$

Using oxygen as an example, c is the dimensionless inhibitor concentration:

$$c = \frac{C_{A0} - C_A}{C_{A0}}, \quad (S5)$$

where C_A and C_{A0} are the concentration and the initial concentration of oxygen in the polymer precursors, respectively (mol/L). Da is the Damköhler number:

$$Da = l^2 \frac{k_0 \int_{\lambda} \alpha(\lambda) I(\lambda) d\lambda}{C_{A0} D_A}, \quad (\text{S6})$$

where l is voxel size (m), D_A the diffusivity of inhibitor (m^2/s), α the absorption coefficient and I the irradiance (mW) of wavelength λ (nm), k_0 is the zeroth order rate constant that relates inhibitor consumption to irradiation. Da evolves spatiotemporally as a consequence of changing irradiation angle and nonlinear polymer response. The Fickian fluxes N_A for each voxel were computed at the six inter-voxel surfaces and photochemical reactions were treated as a zeroth order sink for oxygen, first order sink for *o*-Cl-HABI and second order sink for lophyl radicals. Treating the photolysis of *o*-Cl-HABI as first order reaction allows us to account for the limited capacity of lophyl radical generation. Concentration was assumed uniform inside each voxel. Reactive transport was simulated to assist experimental trial-and-errors for determining optimal exposure time. Simulation was not part of the iterative sinogram computation. Movies S1 and S9-11 were results of numerical simulations.

Supplementary Text

Characteristics of binary photoinhibition

The BPI scheme presented in the main text offers a means to navigate the phase diagram for each voxel individually by adjusting the strength of irradiation using two coordinated light sources (I_{UV} and I_{vis}). Given an illumination profile, the steering trajectory depends on three parameters

$$\alpha = k_{0,B,vis} / k_{0,A,vis}, \quad (\text{S7})$$

$$\beta = \frac{k_{0,B,UV} I_{UV}}{k_{0,A,vis} I_{vis}}, \text{ and} \quad (\text{S8})$$

$$\lambda = \ln 2 / k_{1,B}. \quad (\text{S9})$$

Fig. S20 compiles the influences of these parameters. The parameter α marks the relative sensitivity of the two inhibitory species to visible light, whereas β represents the strength of UV as the pseudo-negative illumination. Greater α indicates greater energy requirement in order to create an unpolymerized stationary state (SS). The difference between a polymerizing SS and an unpolymerized SS is more pronounced with greater β (UV irradiance) as well as a longer half-life for B (λ). In practice, the irradiation received by a voxel varies periodically due to the rotation of the curing volume, and the system status is steered temporally. Movie S1 shows an example of how phase diagram evolves at a constant projector output when a voxel in question is not located at the rotation axis. We define the efficiency of UV as PNI using

$$W = \int_{\varepsilon}^1 \frac{C_B}{C_A} d\left(\frac{C_A}{C_{A0}}\right), \quad (\text{S10})$$

where the lower limit of the integral ε is the normalized concentration of Species A that would initiate polymerization in the absence of B. When $W = 1$, a BPI doubles the induction period before

a voxel polymerizes, and the UV matches the visible light by delivering negative illumination with the same intensity unit, i.e., a sinogram containing both signs can be divided into a positive part and a negative part without additional adjustment of grayscale intensity. Light extinction in the curing volume, however, creates spatial variance of W . Fig. S21 shows the impact of extinction coefficient (μ) on achievable W at five different radial positions, when absorption is not the main cause for light attenuation. The scattered data were obtained by tracking voxels at a fixed radial position but a randomized starting angle. The closer a voxel is to the edge of the curing volume, the more sensitive its W will be to the rotation periodicity. At constant UV output, negativity efficiency reduces towards the rotation center. This spatial loss of efficiency cannot be compensated by simply increasing the output power because the diffusion of excessive radical scavengers generated at large radial distances will cause undesired underexposure. As a result, formulating a BPI can be demanding in that it requires good balance between transparency and absorptivity in at least two wavelength regimes.

In contrast to photoinhibitors used in more conventional light-based additive manufacturing methods, a stable Species B with a long lifespan is favored in BPI because of its cumulative nature of the latter. Fig. S22 shows the impact of half-life on achievable W at three radial positions at constant UV irradiation. The energy that powers the UV irradiation is spent to counteract the overspent doses of visible light that would lead to over-exposure. As a result, a dual color printer uses more energy than its single-color counterpart for printing the same geometry. The UV doses needed to reach $W = 1$ in Fig. S23 shows the sensitivity of the minimum energy requirement for producing equivalent negative illumination across the curing volume for three extinction factors.

Deviation from an ideal binary photoinhibitory system

The oxygen-lophyl system we employed to demonstrate the advantages of a BPI differs from the ideal BPI system in that the lophyl-generation capacity of the photoresin under external stimulus is limited. A prerequisite for indefinitely pinning the binary system at an SS other than the origin is an unlimited supply of Species B upon UV illumination. An abundant supply does not guarantee more efficient negativity generation, as the lifespan of Species B often becomes the bottleneck, but a shortage of supply prevents a BPI from properly functioning (Fig. S24). In this study, the lophyl radical that served as Species B was generated from photolysis of *o*-Cl-HABI. We found that 1 wt% *o*-Cl-HABI (recipe M-1) sufficed to generate lophyl radicals that clearly demonstrated the advantages of a BPI. Higher concentrations led to stronger light extinction (Fig. S25) that would deteriorate workpiece fidelity towards the rotation center.

We measured the absorbance of M-1 resin using UV-Vis spectroscopy, and UV illumination at 70 mW/cm² for 15 seconds did not deplete the *o*-Cl-HABI (Fig. S26A). Also, lophyl recombination did not follow a first order law and therefore did not have a constant half-life. However, its decay is sufficiently slow to be cumulative during printing. The generation of lophyl does follow a zeroth order kinetic regarding UV illumination and upscales with the power of irradiance (Fig. S26B). It remains unclear how the competition between oxygen and lophyl for visible light scales with their relative concentration ($RC = [\text{Oxygen}] / [\text{Lophyl}]$). However, the prolonged induction period due to lophyl's presence varied according to the timing of introducing UV (Fig. S12). When 30 seconds of UV illumination was introduced before visible light, the induction period was prolonged from 30 s to 38 s. When the same UV illumination was introduced after 30 seconds of visible light illumination, the induction period was instead prolonged to 50 s. The latter represents a case with a relatively lower RC , and the extended induction indicates that

the consumption of visible dose by lophyl radicals does correlate positively with its relative concentration to oxygen – in the second case, more lophyl was consumed at a low RC and thus less was lost to self-recombination. Co-illumination of both sources was employed to minimize the effect of self-recombination, and the inductive period was further prolonged to 68 s.

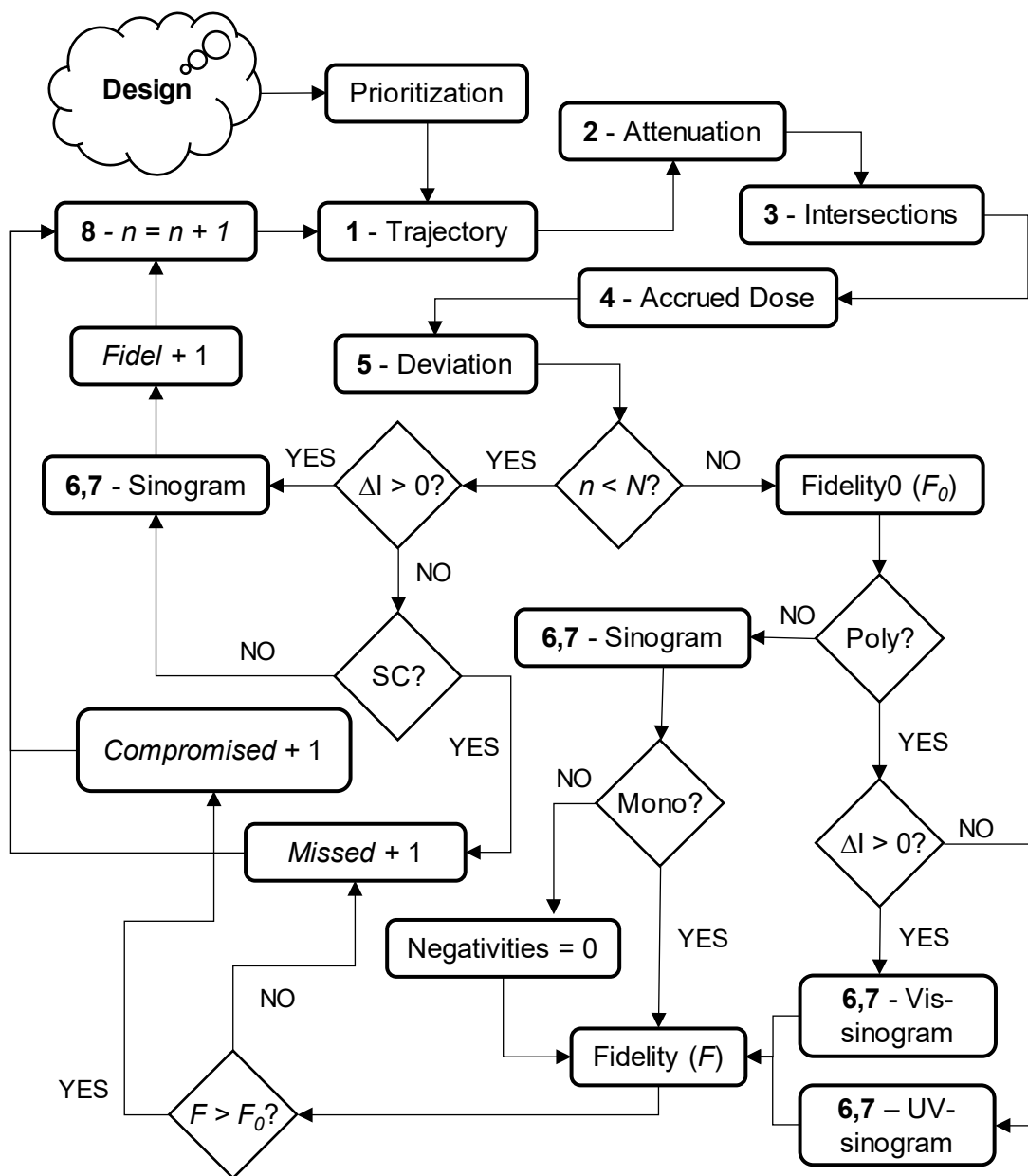


Fig. S1. The eight-step protocol for sinogram generation. When the total number of voxels exceeds the allowed design freedom, the difference schemes (SC, DC-mono, DC-poly) branch into different actions and results in different degrees of fidelity loss.

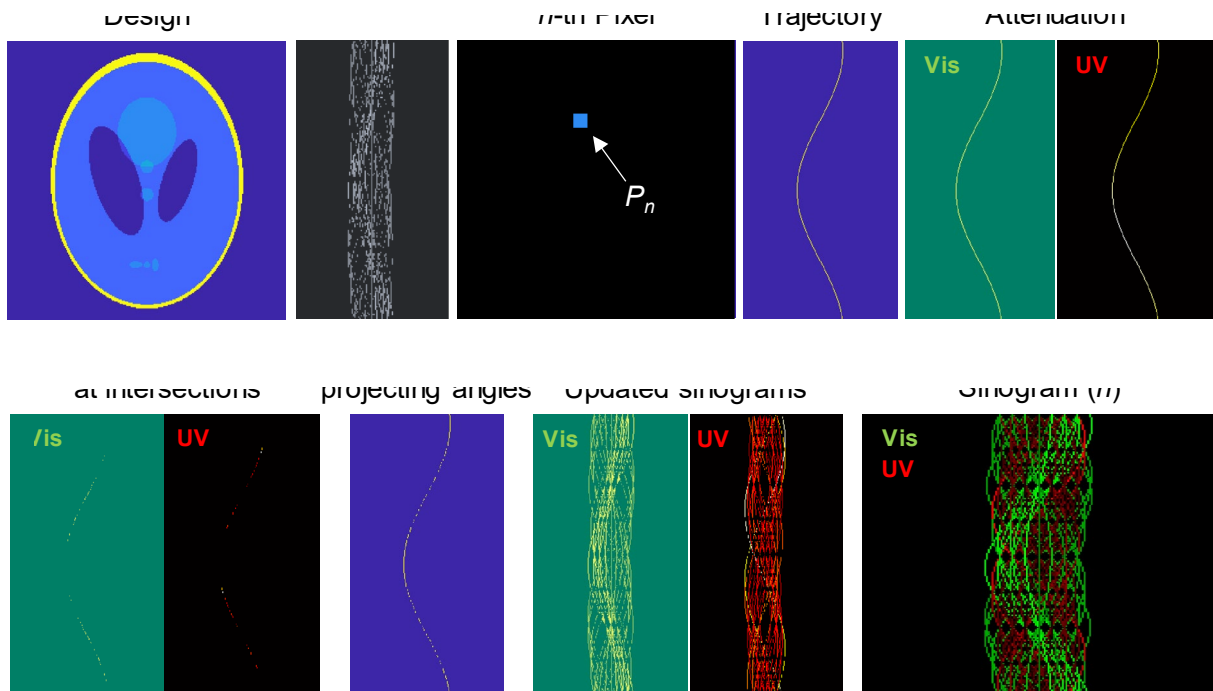


Fig. S2. Exemplary stepwise outcomes during sinogram computation if the eight-step protocol is followed.

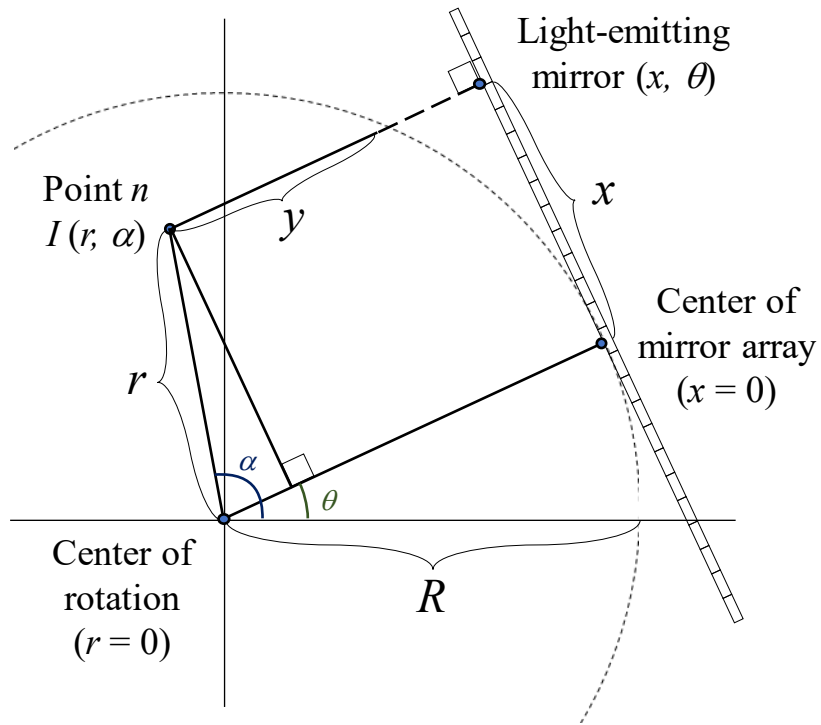


Fig. S3. Geometric drawing of the parallel beam assumption employed in the eight-step protocol.

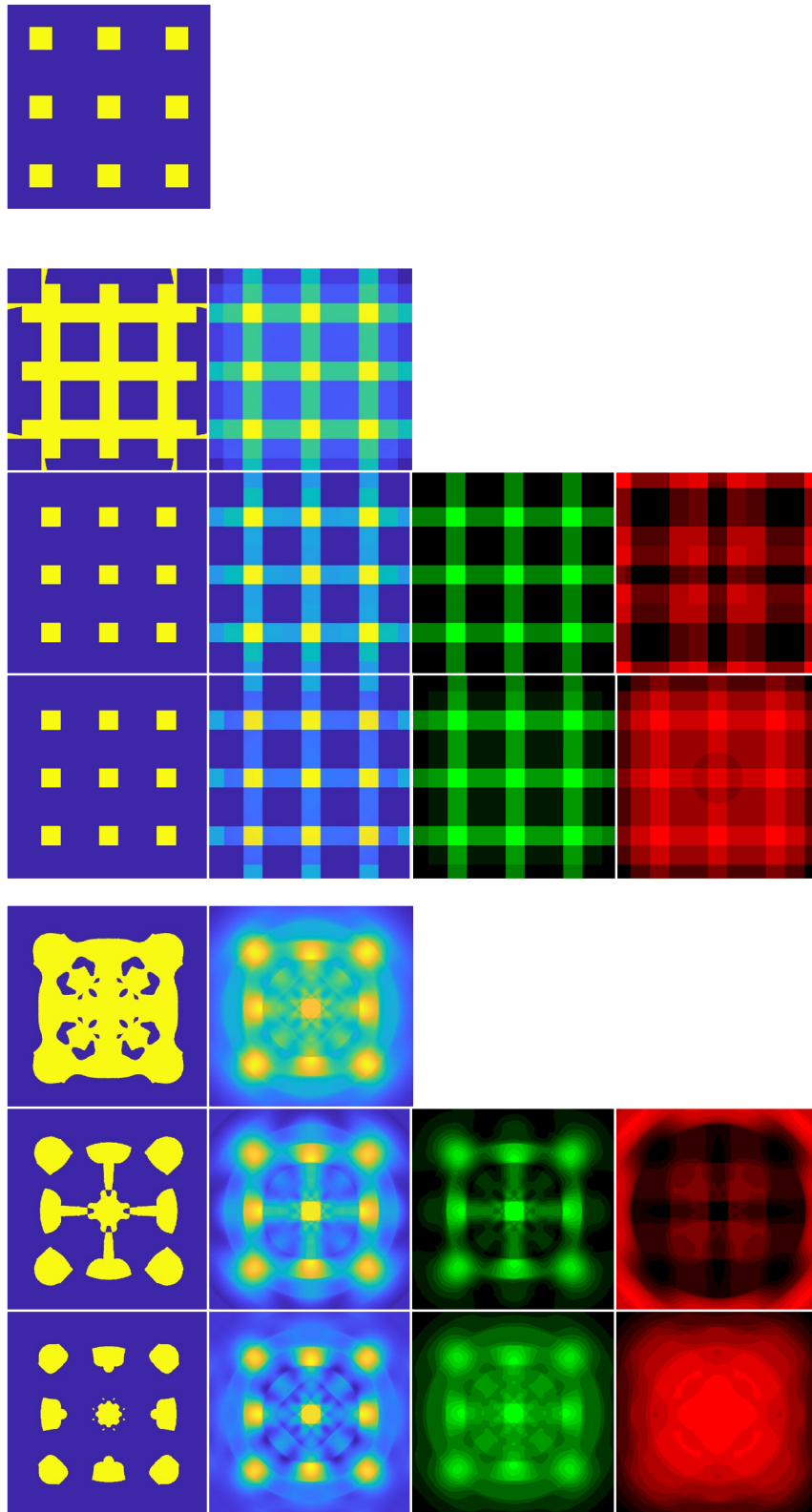


Fig. S4. Effective dose built-ups at two levels of design freedom ($N = 2, 360$).

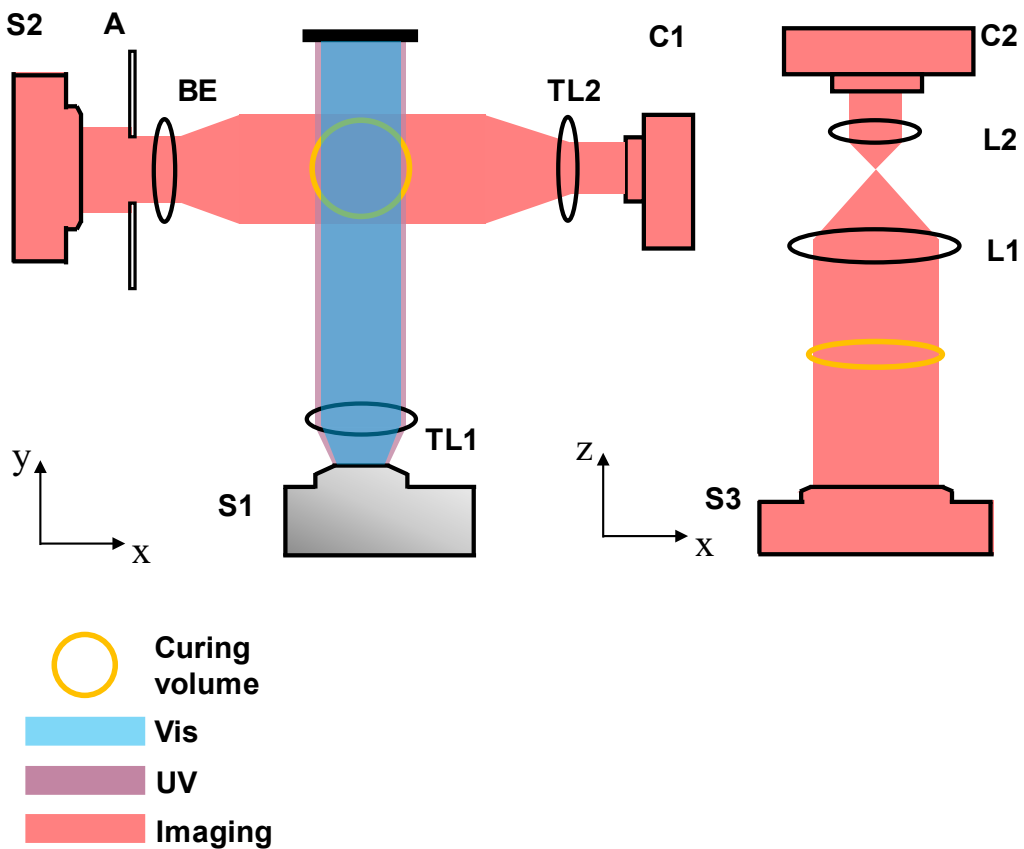


Fig. S5. Schematic illustration of the dual-color tomographic volumetric printing modality.
 All parts are tabulated in Table S2.

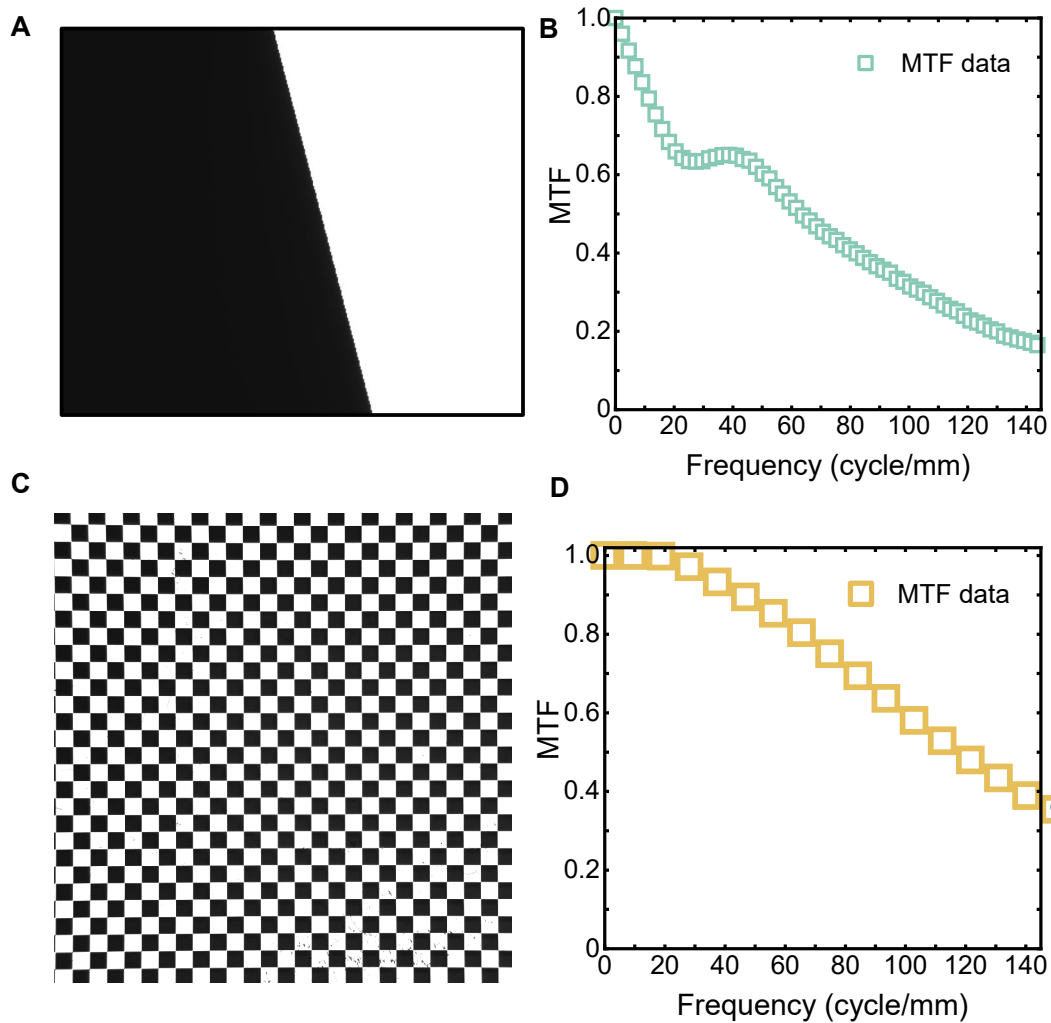


Fig. S6. Characterization of optical modulation transfer function (MTF). (A) Projected slanted-edge image captured by the detector at focal plane. (B) MTF data of the projector optical system calculated with ImageJ. (C) Imaging of checkerboard calibration target at focal plane captured by detector. (D) MTF data of the lateral imaging system.

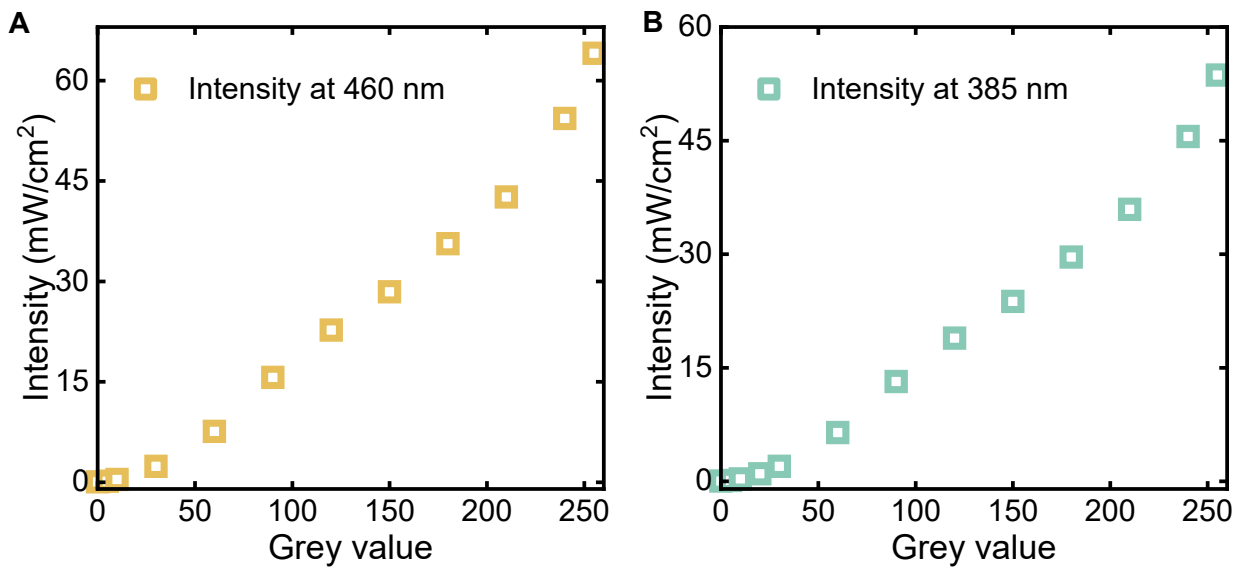


Fig. S7. Irradiation intensity as a function of pixel grey value. Irradiance was measured at the focal plane using a photodiode power sensor. (A) Irradiation from S1 at 460 nm. (B) Irradiation from S1 at 385 nm.

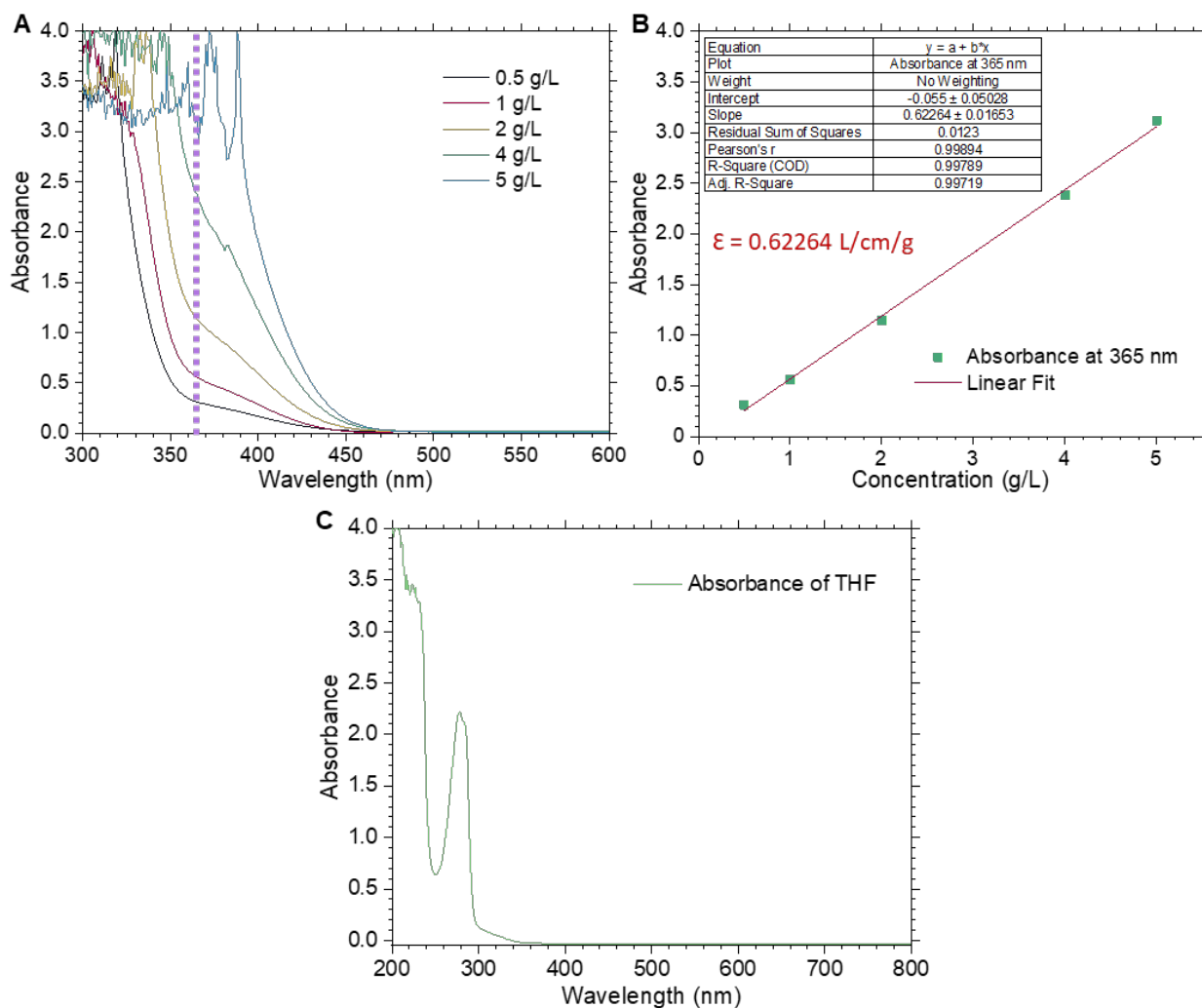


Fig. S8. UV-Vis spectroscopy for *o*-Cl-HABI and THF. (A) Absorption profiles at various *o*-Cl-HABI concentrations. **(B)** Fitted absorption data for calculating extinction coefficient at 365 nm. **(C)** Absorption profile of the solvent THF. There is no absorption of THF near 365 nm or in the visible range, indicating that the effect of THF on the optical properties of the photoresin associated with tomographic printing is limited.

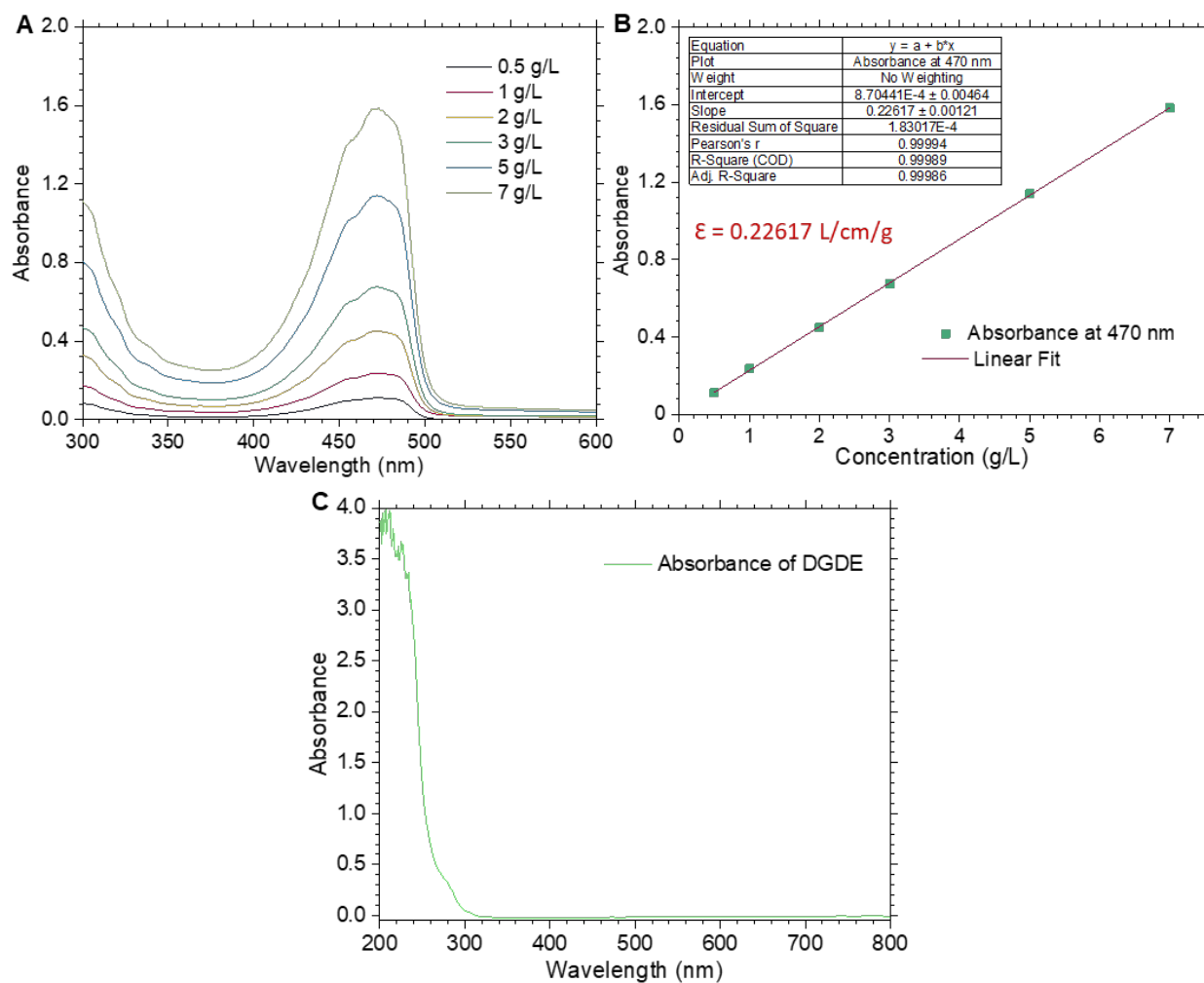


Fig. S9. UV-Vis spectroscopy for CQ. (A) Absorption profiles at various CQ concentrations. (B) Calculation of extinction coefficient of CQ at 470 nm. (C) Absorption profile of the solvent DGDE, no absorption in the visible wavelength regime was identified.

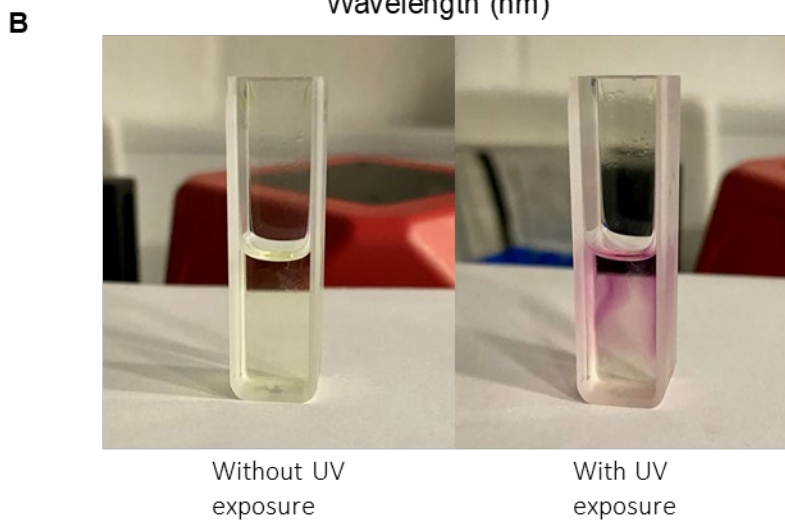
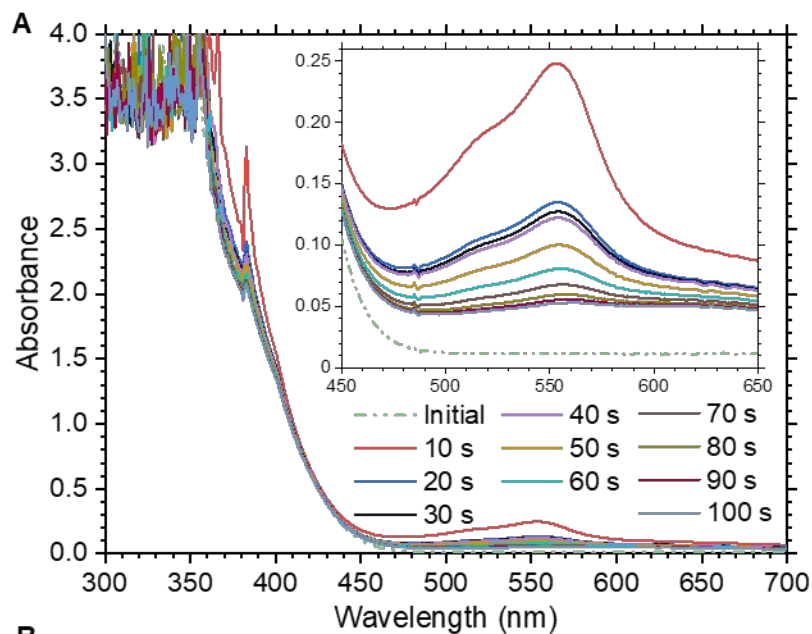


Fig. S10. UV-Vis measurement of the *o*-Cl-HABI solution after UV illumination. (A) After the initial measurement, the sample was illuminated by UV for 30 s at 30 mW/cm², after which an absorbance spectrum was taken every 10 s. The peak near ~555 nm correlates with the transient lophyl concentration and is zoomed-in in the inset. **(B)** Color change upon *o*-Cl-HABI photolysis corresponding to the peak near 550 nm.

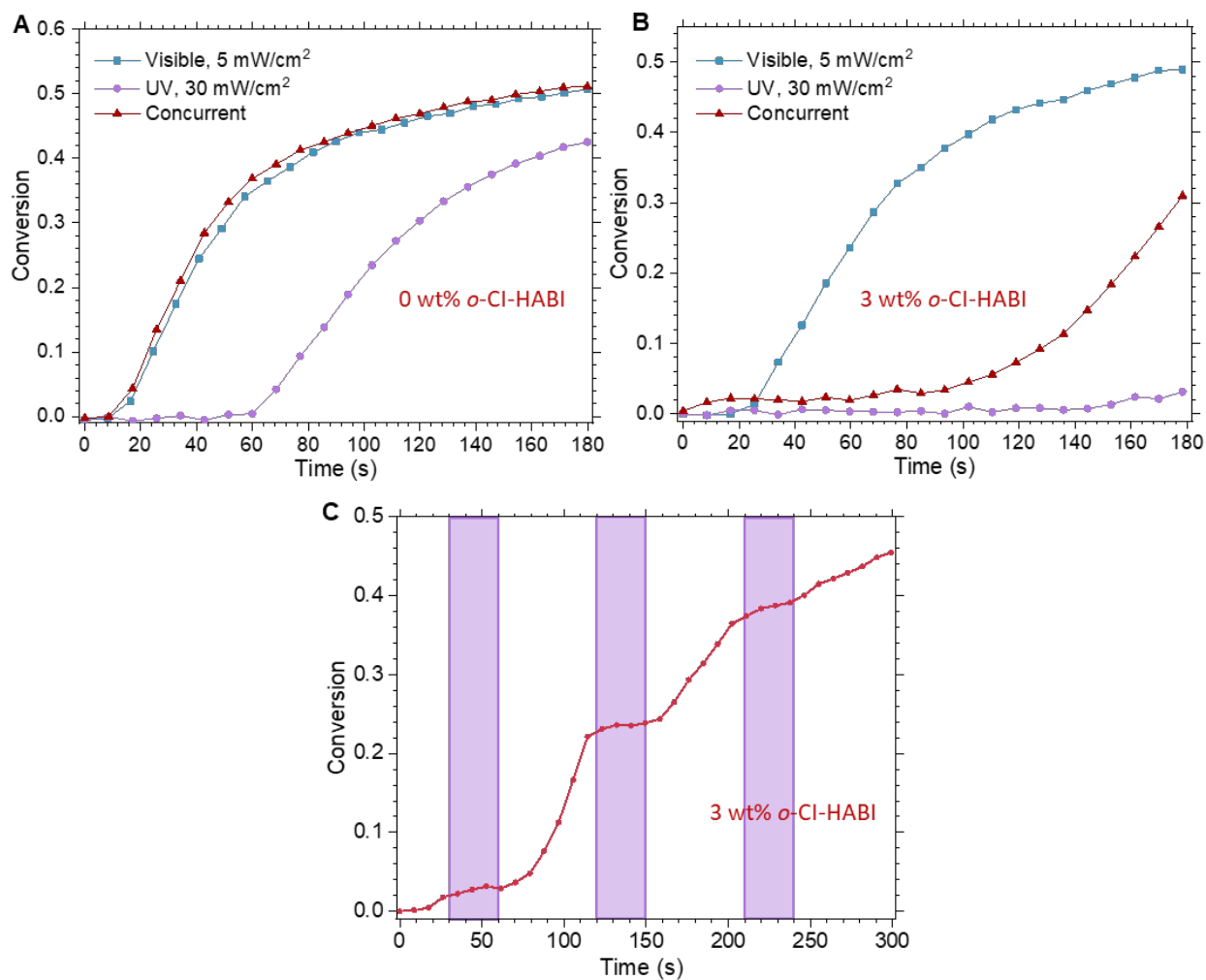


Fig. S11. Double bond conversion upon illumination. The irradiance of visible and UV light were 5 mW/cm² and 30 mW/cm², respectively. “Concurrent” means both sources were on. **(A)** without *o*-Cl-HABI; UV led to polymerization because of the weak UV absorption induced by CQ. **(B)** Conversion in M-3. UV prolonged the inductive period. **(C)** Resin M-3 was illuminated continuously by visible light, and intermittently by UV (shaded, 30 s each). UV could not revert the polymerization but could effectively arrest the conversion.

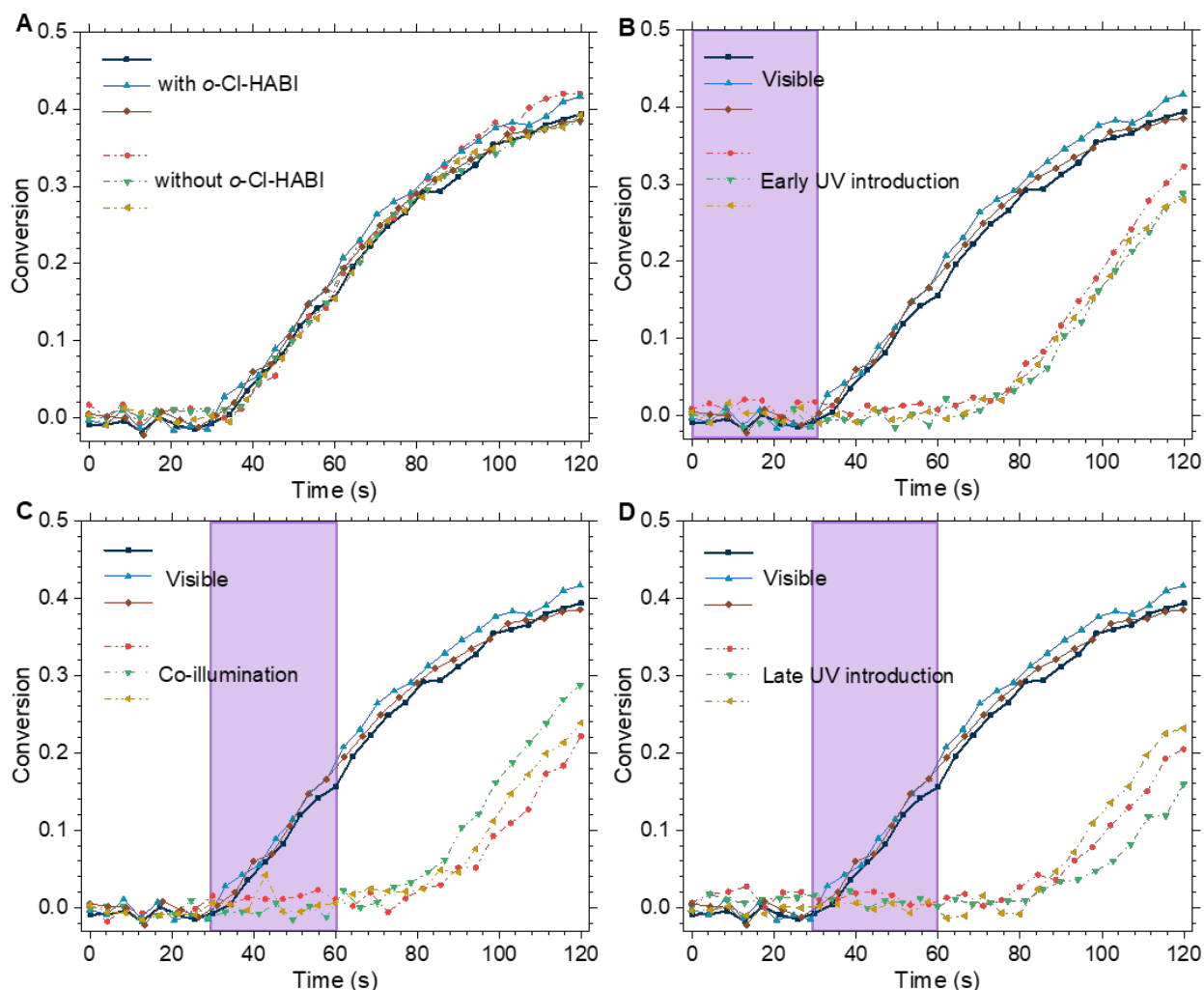


Fig. S12. Sensitivity of conversion to the timing of UV illumination. The irradiance of visible and UV light were 3 mW/cm^2 and 30 mW/cm^2 , respectively. (A) No UV illumination. Solid lines: Resin M-3; dashed lines: without *o*-Cl-HABI. The induction was ~30 s. (B) Early UV introduction (M-3). Solid lines: no UV. Dashed lines: resin illuminated by UV for 30 s (shaded) before introducing visible light. Induction period was ~38 s. (C) Co-illumination (M-3). Solid lines: no UV. Dashed lines: continuously illumination from visible light source with 30 s of UV co-illumination (shaded). Induction period was ~68 s. (D) Late UV introduction (M-3). Solid line: no UV. Dashed lines: resin illuminated by visible light source alone for 30 s, then by UV alone for another 30 s (shaded), then by visible light again until crosslinking. Induction was ~50 s. All tests were repeated 3 times.

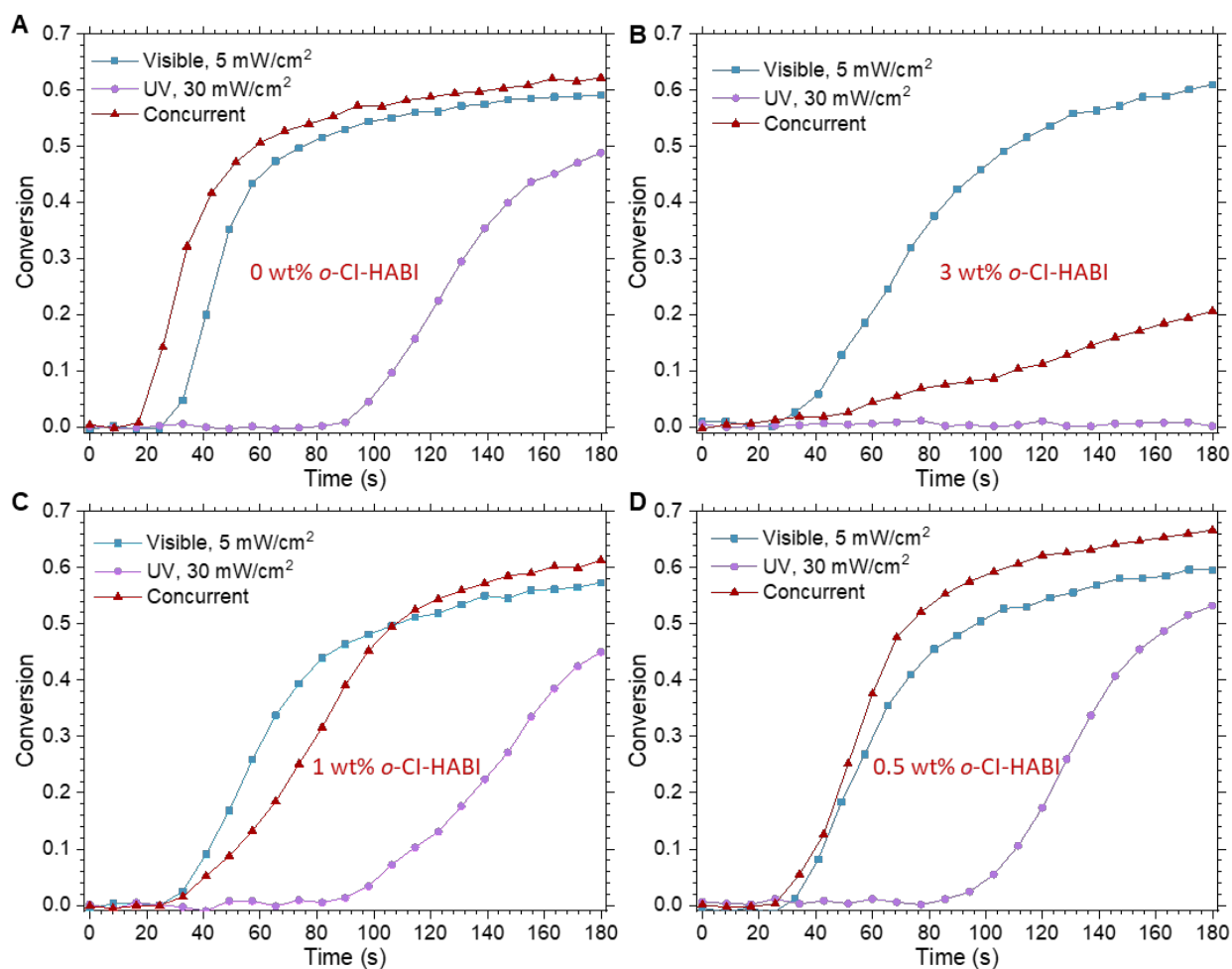


Fig. S13. Sensitivity of double bond conversion to illumination for diacrylate-based resin at various *o*-Cl-HABI concentrations. The irradiance of visible and UV light were 5 mW/cm² and 30 mW/cm², respectively. “Concurrent” means both sources were on. **(A)** Resin A250 (without *o*-Cl-HABI). **(B)** Resin A250-3 (3 wt% *o*-Cl-HABI). **(C)** Resin A250-1 (1 wt% *o*-Cl-HABI). **(D)** Resin A250-0.5 (0.5 wt% *o*-Cl-HABI). Higher concentration of *o*-Cl-HABI was needed to delay gelation or inhibit conversion of the BPAGDA/PEGDA resin.

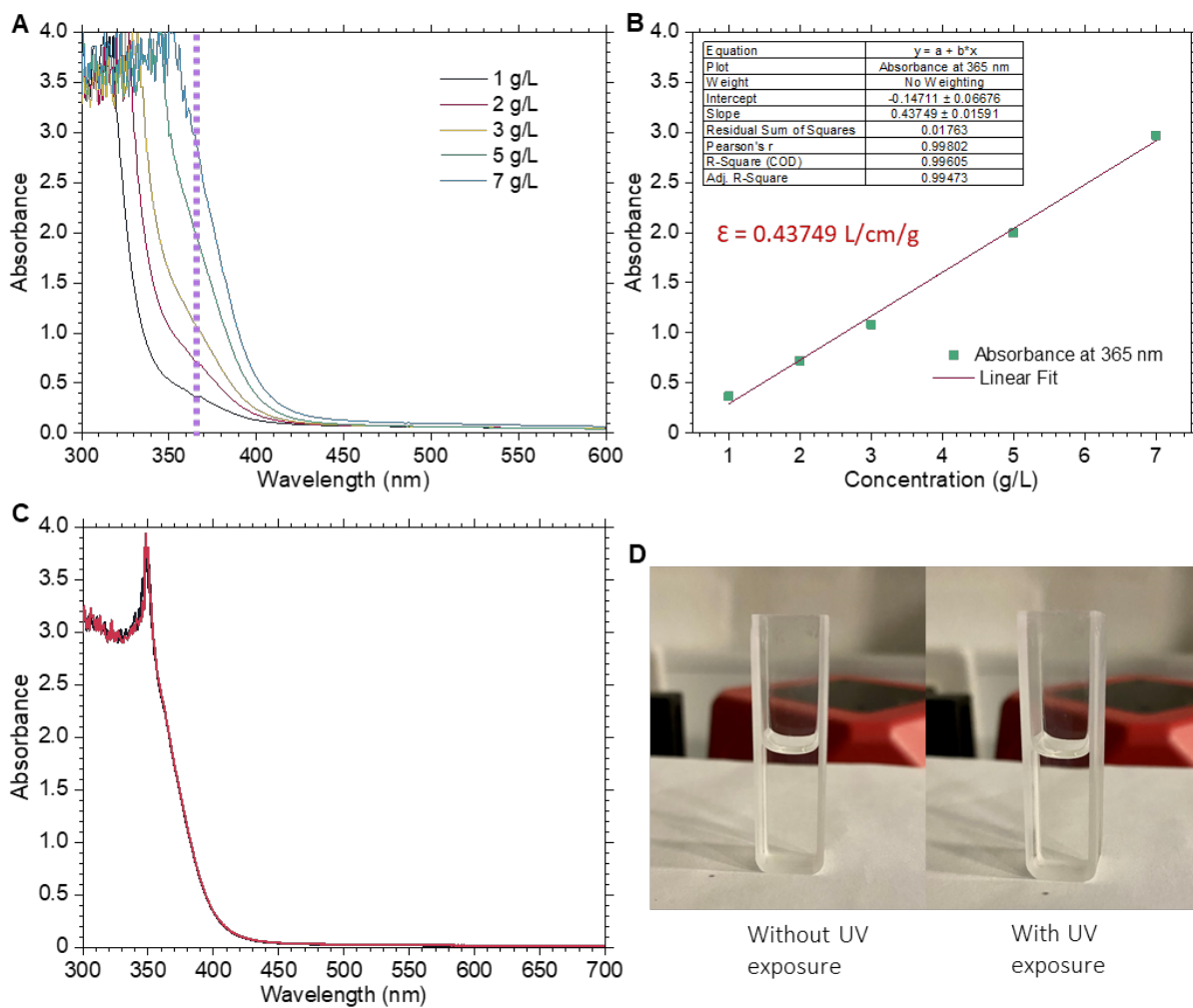


Fig. S14. UV-Vis spectroscopy for tetraethylthiuram disulfide (TED, CAS#97-77-8, Sigma-Aldrich) in THF. (A) Absorption profiles at various TED concentrations. **(B)** Calculation of extinction coefficient of TED at 365 nm. **(C)** Measurement of the absorption data of the 5 g/L TED in THF in the state without (black line) and with (red line) UV exposure, indicating that there is no absorption change upon UV introduction. **(D)** No color change upon TED photolysis.

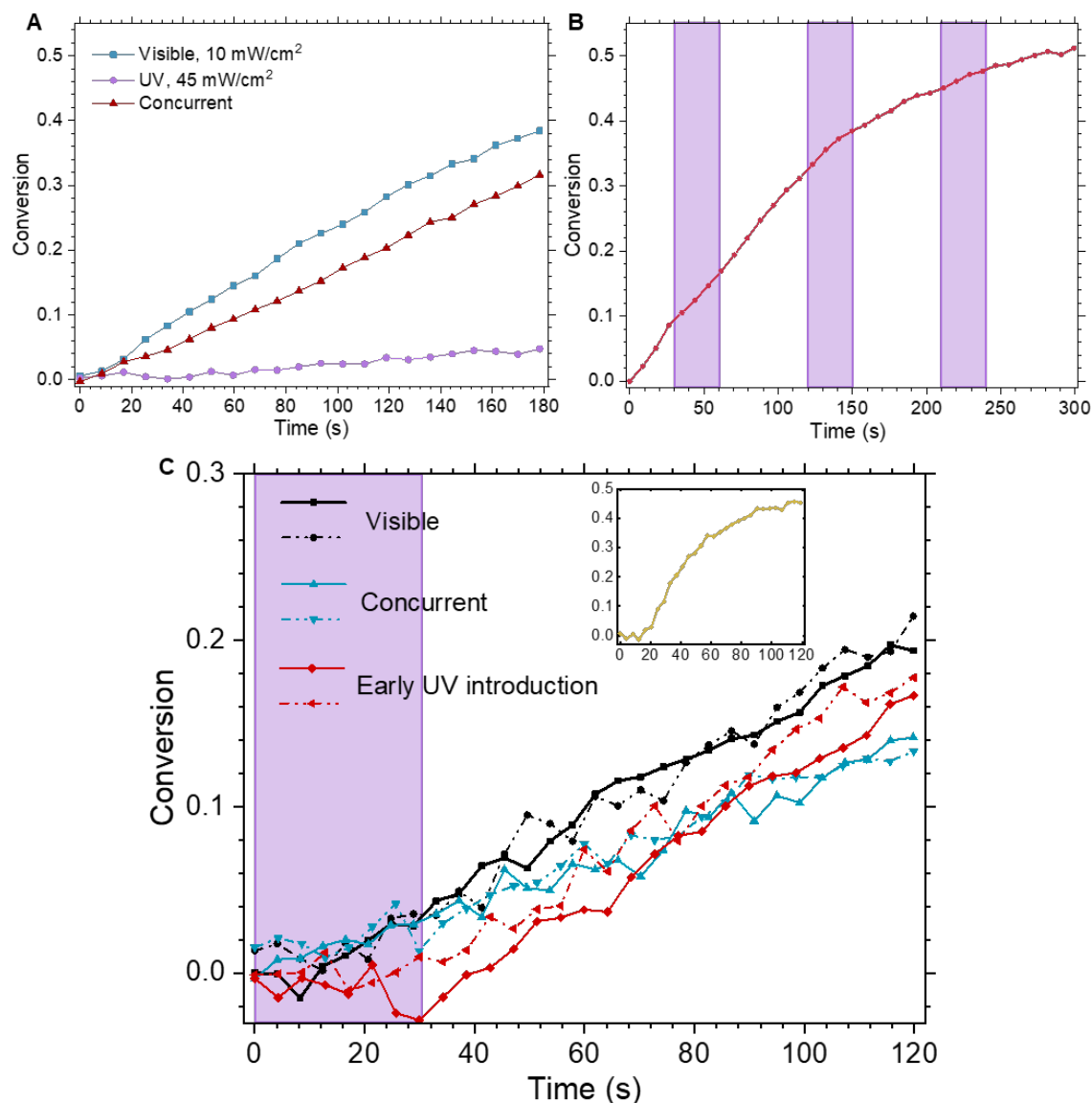


Fig. S15. Double bond conversion upon illumination for methacrylate-based recipe with 3 wt% TED added as inhibitor. “Concurrent” means both sources were on. (A) Conversion in the resin. The irradiance of visible and UV light were 10 mW/cm² and 45 mW/cm², respectively. (B) Resin was illuminated continuously by visible light (10 mW/cm²), and intermittently by UV (45 mW/cm², shaded, 30 s each). UV weakly arrested the conversion. (C) Sensitivity of conversion to the timing of UV illumination. The irradiance of visible and UV light were 5 mW/cm² and 30 mW/cm², respectively. Black lines: continuous visible light without UV; Blue lines: concurrent visible and UV light; Red lines: early UV introduction for 30 s (shaded) before introducing visible light. UV could not extend the induction period and only mildly inhibited the conversion. Inset shows the conversion of resin without TED under continuously visible light. TED may significantly reduce the polymerization rate of resin.

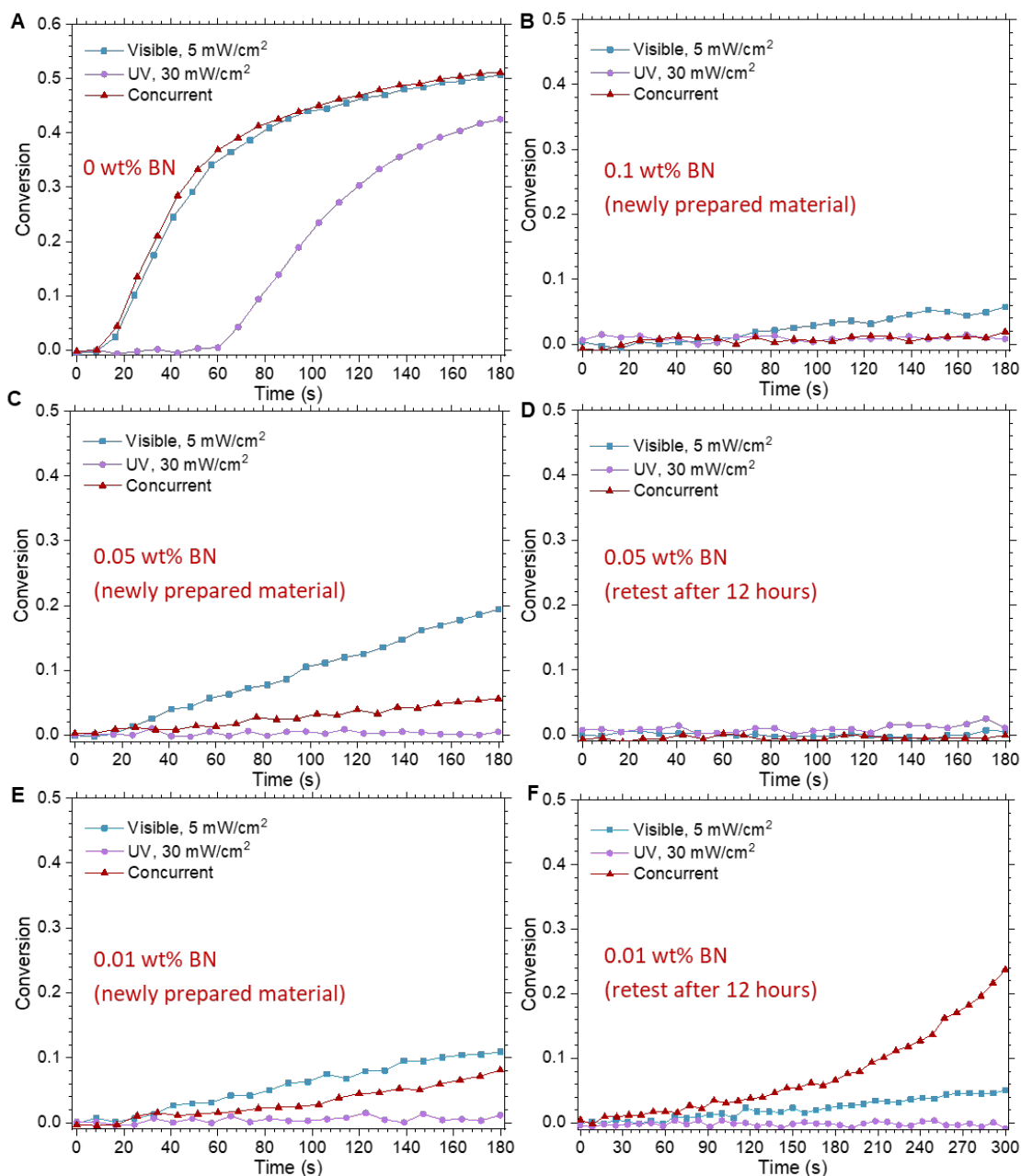


Fig. S16. Sensitivity of double bond conversion to illumination for methacrylate-based recipe at various of butyl nitrite (BN, CAS# 544-16-1, Sigma–Aldrich) concentrations. BN was used as inhibitor and added to the methacrylate-based formula. The irradiance power of visible and UV light were 5 mW/cm² and 30 mW/cm², respectively. (A) without BN. (B) 0.1 wt% BN, Measurement was carried out using the newly prepared material (C) 0.05 wt% BN. (D) 0.05 wt% BN, retested after 12 hours; It shows the different results from that in figure (C). (E) 0.01 wt% BN. (F) 0.01 wt% BN, retested after 12 hours.

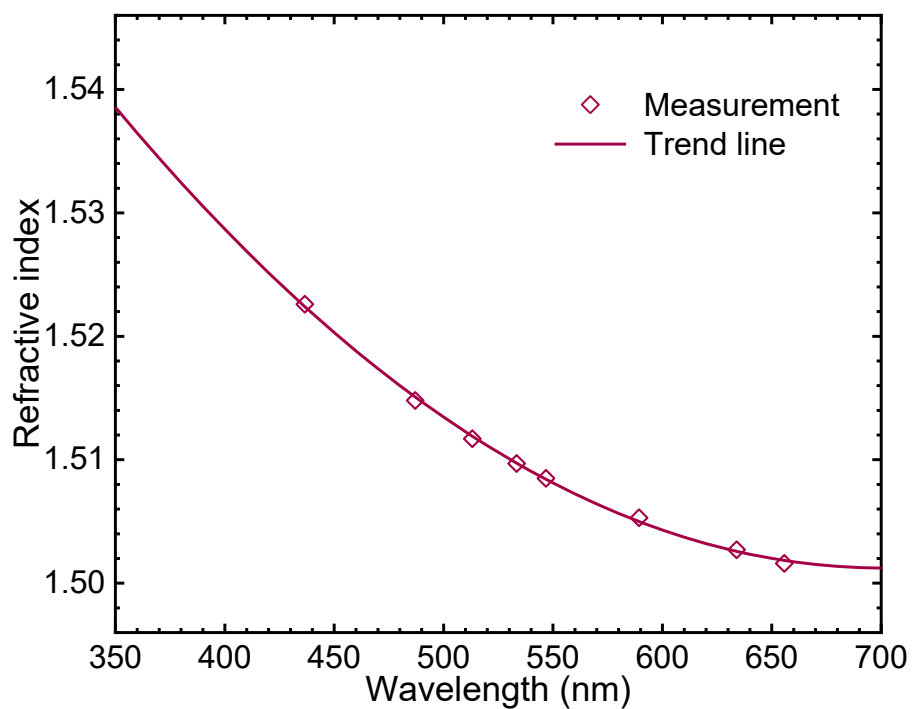


Fig. S17. Refractive indices of Resin M-1. Refractive indices were measured using an Abbe refractometer (Anton Paar, Austria). Trendlines are added as visual aid.

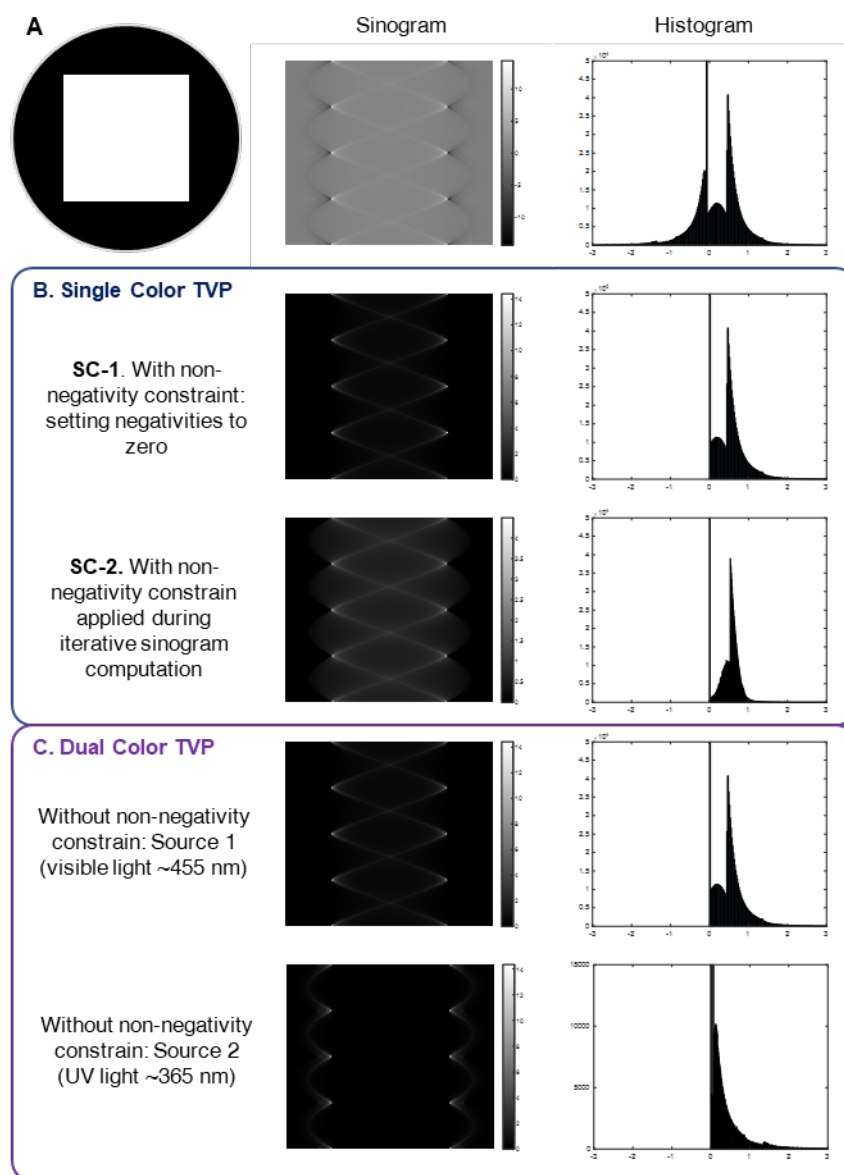


Fig. S18. Impact of non-negativity constraint. (A) A square and its sinogram computed using the iterative method. The sinogram contains negativities that erase undesired energy build-up. (B) Two methods of handling negativity in single color printing. SC-1: setting all negativities to zero; SC-2: non-negativity constraint applied in each iteration during sinogram computation. SC-2 was employed in our previous study (5). (C) With binary photoinhibition, the positive part of the original sinogram is projected by the visible light source (S1) and the absolute values of the negativities are projected by the UV light source (S2).

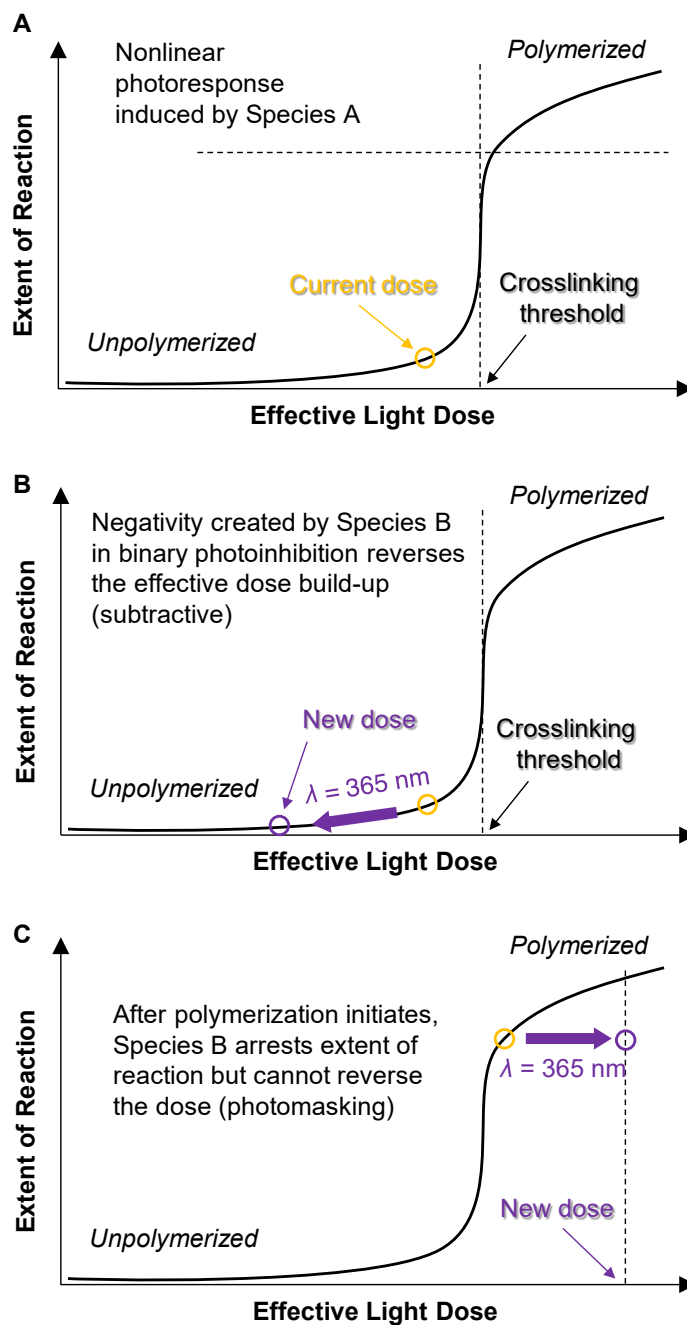


Fig. S19. Photochemical negativity vs. photomasking. (A) The nonlinear photoresponse required for tomographic printing can be introduced using a single photo inhibitor. (B) Photochemical negativity created via binary photoinhibition reverses the system state along the nonlinear curve, amounting to reducing effective dose build-up, i.e., the effect is subtractive. (C) After polymerization initiates, Species B can only arrest the extent of reaction but not reversing it (photomasking).

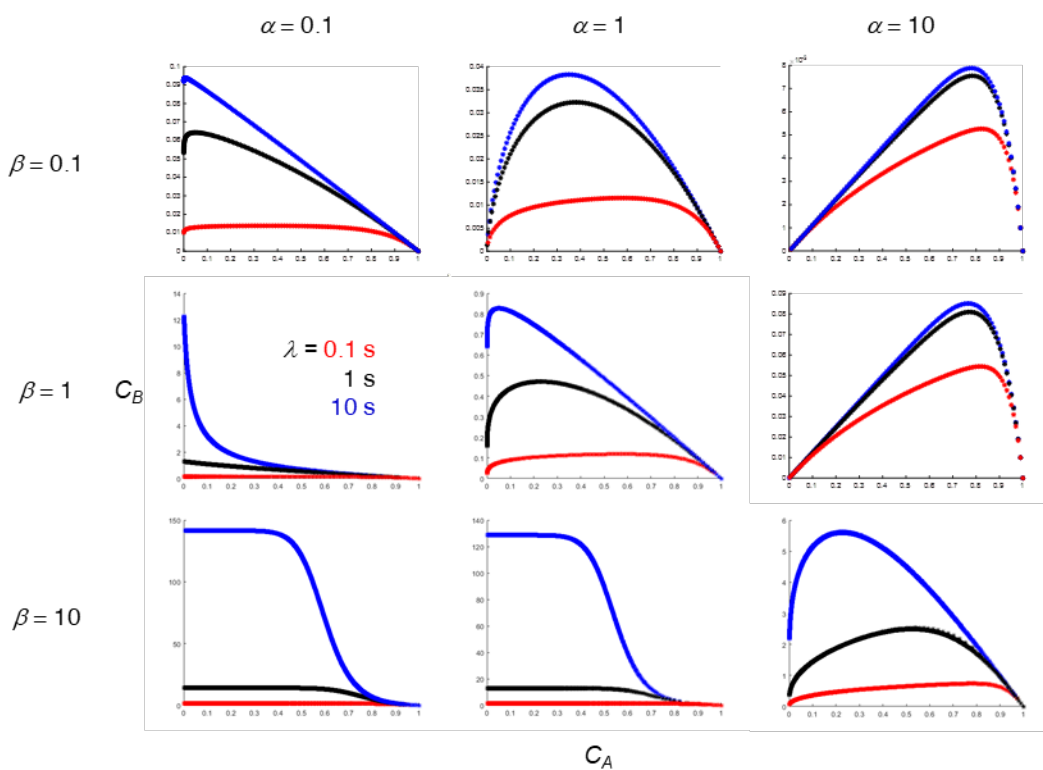


Fig. S20. Sensitivity of system trajectory to kinetic parameters. α represents the relative sensitivity of the two radical scavengers to visible light illumination. β represents the relative strength of irradiation from the two sources. λ is the half-life of Species B if its decay follows first order kinetic.

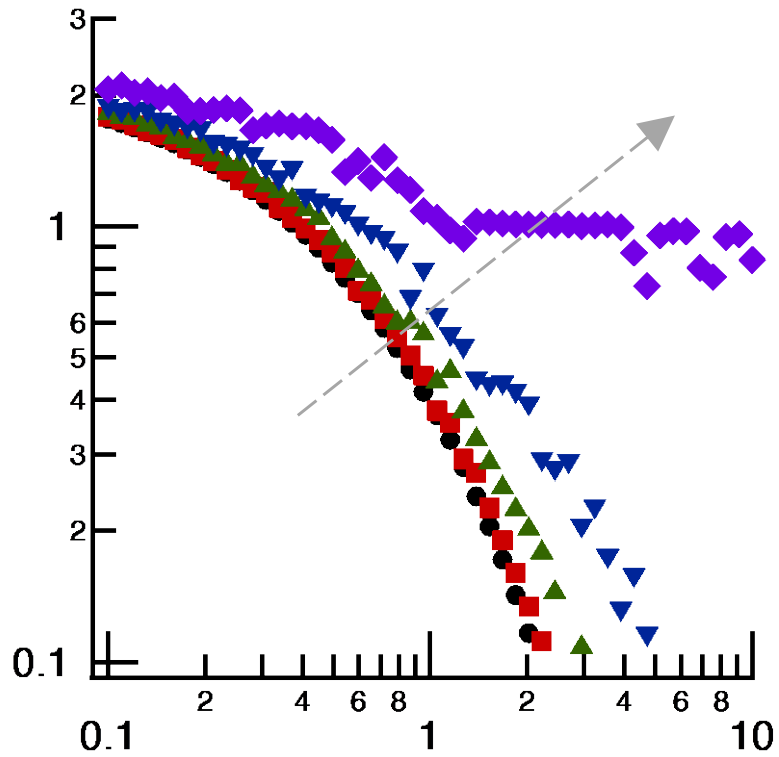


Fig. S21. Dependence of negativity equivalence (W) on extinction coefficient (μ) at various radial position. Results were obtained from numerical simulations. Each data point corresponds to a simulation of a voxel with a fixed radial position but randomized starting angle. $r/R = 0$ (black), 0.25 (red), 0.50 (green), 0.75 (blue) and 1.0 (purple).

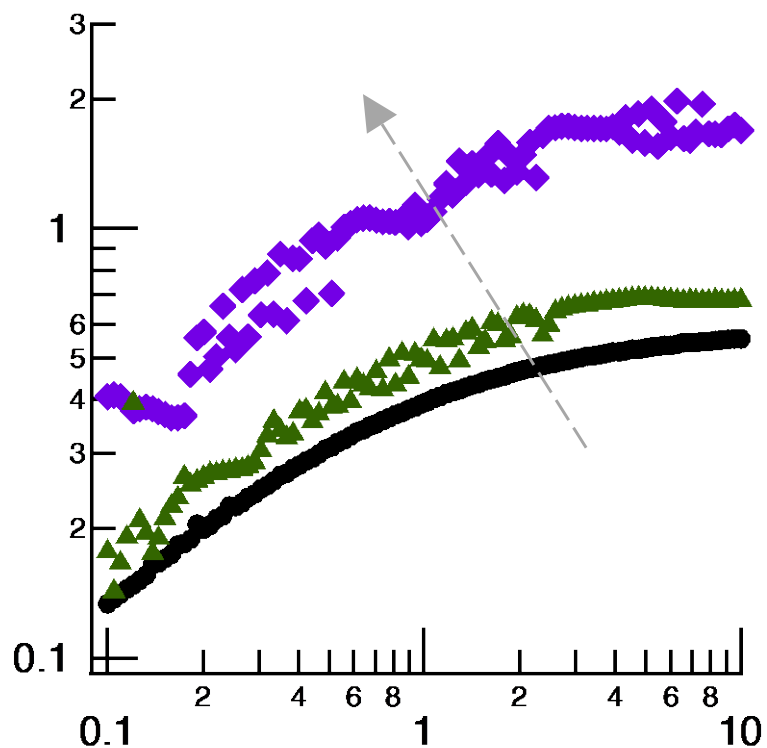


Fig. S22. Sensitivity of negativity equivalence to the half-life of Species B (λ). Results were obtained from numerical simulations. Each data point corresponds to a simulation of a voxel with a fixed radial position but randomized starting angle. $r/R = 0$ (black), 0.50 (green) and 1.0 (purple).

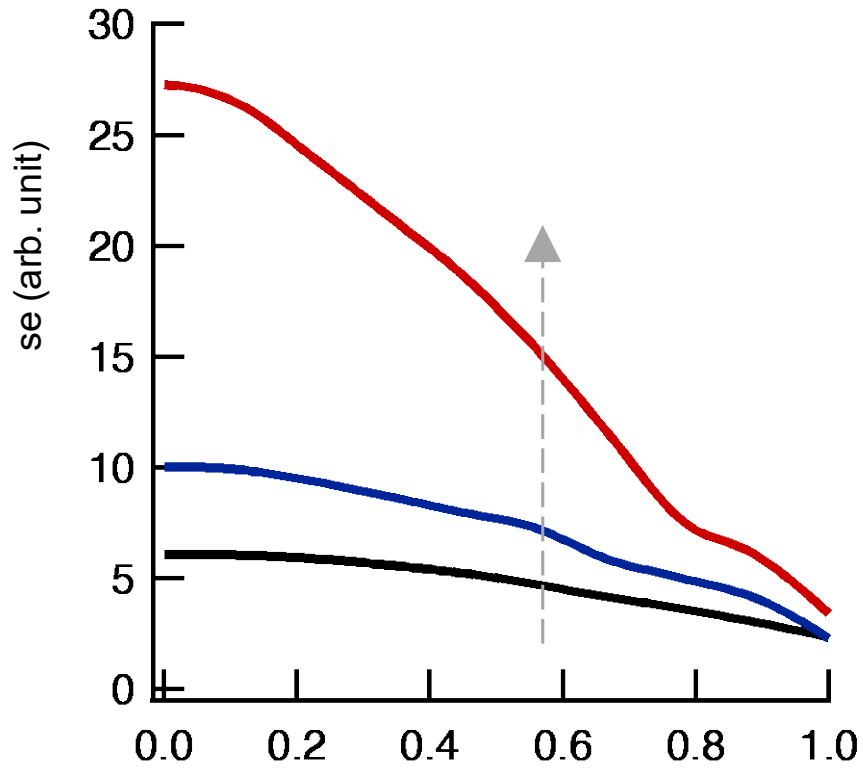


Fig. S23. Sensitivity of energy consumption for achieving unity equivalence ($W = 1$) to radial position. Results were obtained from numerical simulations. Each data point corresponds to a simulation of a voxel with a fixed radial position but randomized starting angle. Three levels of light extinction were tested: $\mu \cdot R = 50$ (black), 100 (blue) and 200 (red).

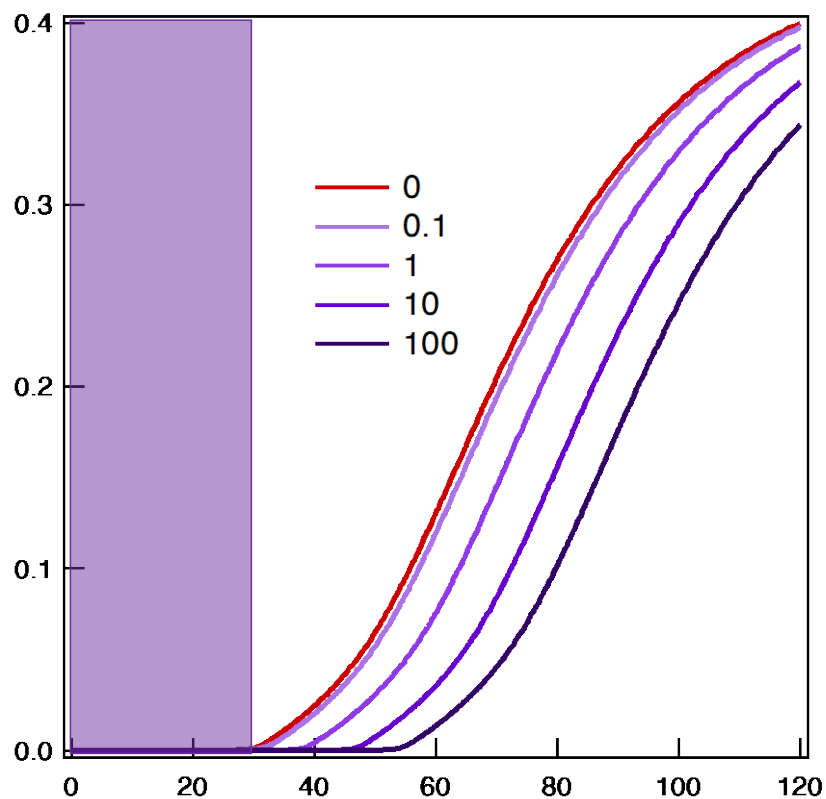
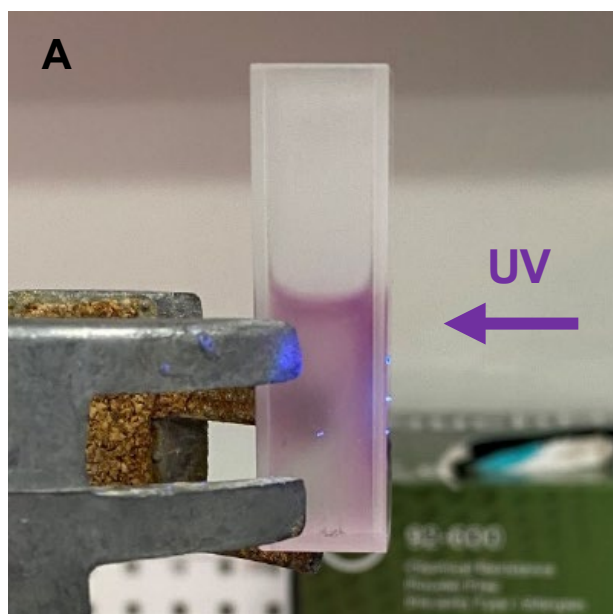
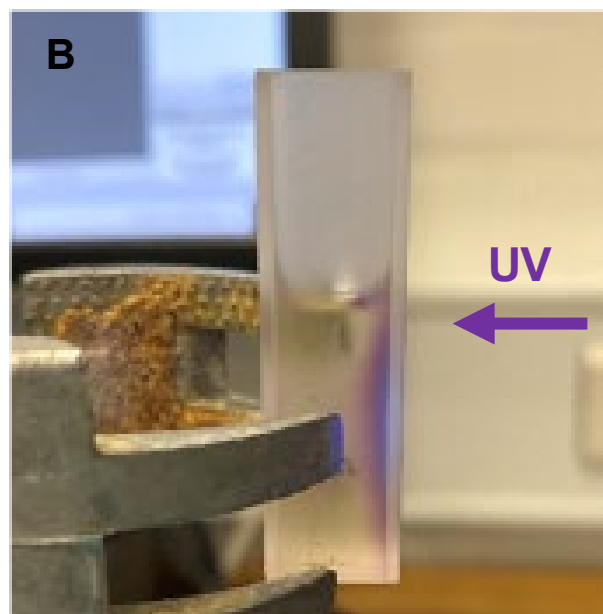


Fig. S24. Simulated effect of Species B-generation capacity on the efficiency of binary photoinhibition. The red line shows the nonlinear photoresponse required for a single-color tomographic printing system to function (only with Species A). Shaded area shows the duration of UV illumination (30 s). Visible light was always on. The capacity is measured as the maximum reachable concentration of Species B compared to the initial concentration of Species A. See Movies S3 & S4 for a simulation in which $C_{B,max}/C_{A0} = 1$.



1 wt% *o*-Cl-HABI (M-1)



3 wt% *o*-Cl-HABI (M-3)

Fig. S25. Effect of *o*-Cl-HABI concentration on light extinction. The purple color indicates the depth to which UV light penetrated into the cuvette and stimulated lophyl radical generation via photolysis.

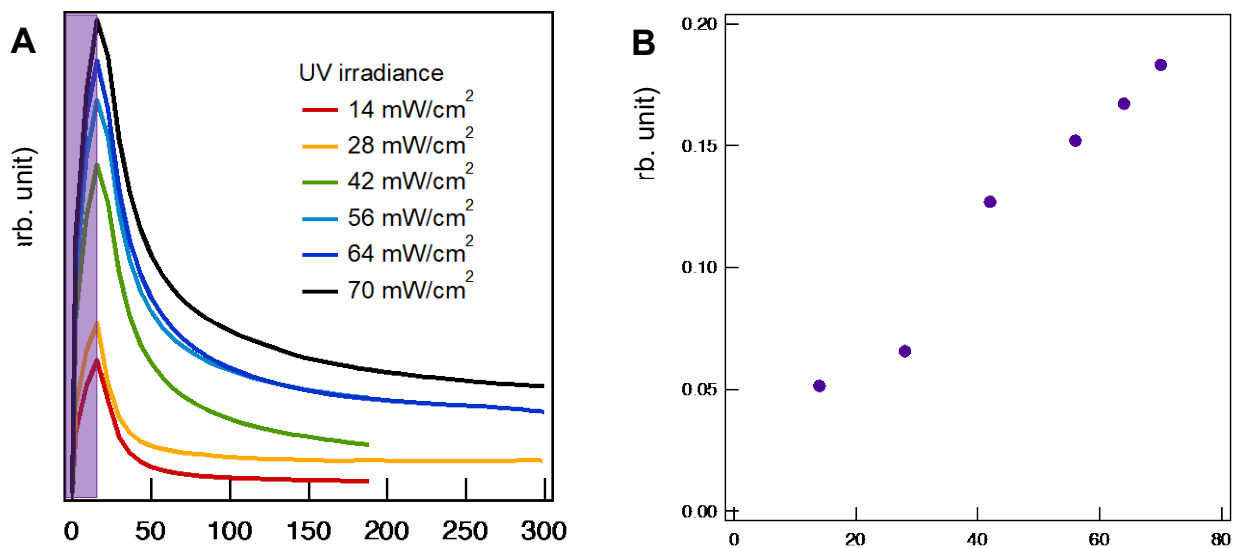


Fig. S26. Generation of lophyl radicals via UV stimulus. Absorbance was measured at 557 nm at an interval of 6.9 s at various stimulating strengths. Resin M-1 was first flushed with white light for 15 s to remove pre-dissolved oxygen, then illuminated by UV at varied irradiance for 20 s. **(A)** The decay of absorbance indicated that the self-recombination of lophyl radicals was slow enough to be comparable with and cumulative in a printing process. **(B)** The maximum absorbance scaled linearly with UV irradiance, indicating good lophyl generation capacity.

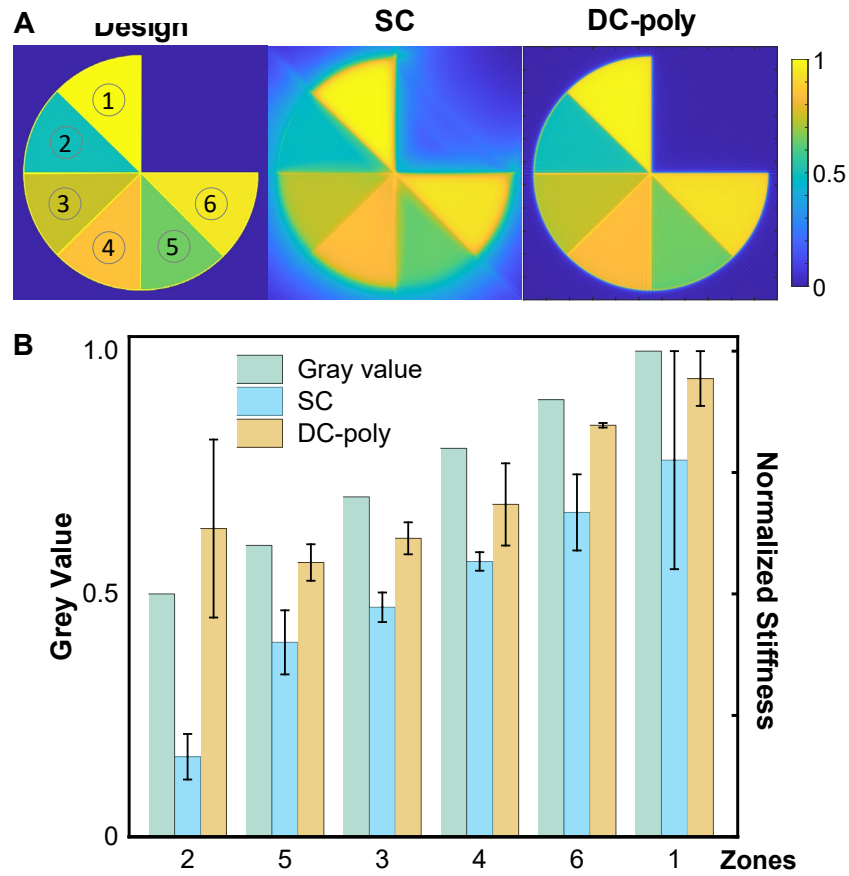


Fig. S27. Greyscale printing. (A) Simulated outcome of greyscale printing a pie chart consisting of six distinct grey values for the SC and DC-poly schemes. (B) Stiffness in various zones measured using a texture analyzer. While both schemes realized greyscale printing, DC-poly offers significantly improved geometric fidelity.

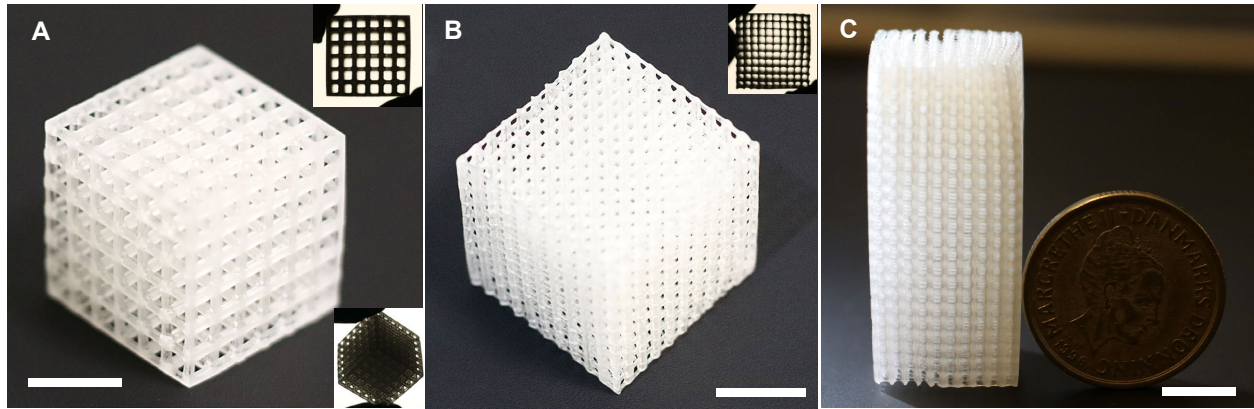


Fig. S28. Lattice structure printed using the SC scheme when $N = 2$. (A) $6 \times 6 \times 6$ cubic lattice, with insets showing the lateral view (top) and the patent compartments (bottom). (B) $10 \times 10 \times 10$ cubic lattice, with inset showing the lateral view. (C) $10 \times 10 \times 20$ cubic lattice. Resin used was 2A250. Scale bars are all 10 mm.

Table S2. Optomechanical components in the dual color tomographic volumetric printer assembly (Fig.S5).

Component identifier in Fig. S1	Component
S1	Xiamen Zhisen TVP07-15-460/385
S2	Thorlabs M625L4-C4
S3	ES technology DH-PX70
C1	FLIR Grasshopper GS3-U3-51S5M-C
C2	FLIR Grasshopper GS3-U3-51S5M-C
A	Thorlabs SM1D12D
BE	Wuhan Baixin D series 5x
TL1	Xiamen Zhisen telecentric lenses
TL2	ES technology ESCM014-180X23
L1	Thorlabs LA1979-N-BK7
L2	Edmund TECHSPEC59-871

Table S3. Differentiable feature counting. The smallest periodical features created at high design freedom ($N = 360$) were manually identified in multiple representative regions of images captured using *in situ* shadowgraphy (Fig. 4A). The pixel pitch of the imaging modality ($27 \mu\text{m}$) and the number of pixels in each row co-determine the maximum size of single feature at different design DPI.

Design DPI	Corresponding Feature Size (μm)	Observable feature using <i>in situ</i> lateral shadowgraphy			
		SC		DC	
		# of pixels	Maximum size of observed feature (μm)	# of pixels	Maximum size of observed feature (μm)
101	251.5	9	243	9	243
169	150.3	6	162	6	162
338	75.1	4	108	3	81
676	37.6	3	81	2	54
1016	25.0	NA	NA	1	27

Movie S1. Transient Stationary State. Evolution of phase diagram at constant illumination as a result of curing volume rotation. τ is the number of full rotations.

Movie S2. USAF. Top view of the printing process of a US Air Force resolution target. The diagonal of the 1500×1500 square design (Fig. 4L) matches the diameter of the printing vial (Ø30 mm, corresponding to a row of 2160 mirror units on DMD). The playback has been accelerated and the actual exposure was around 6 minutes. The entire pattern was printed, and the lateral imaging modality captured the inner (finer) part of the workpiece.

Movie S3. Fall. Top view of the printing process of an artistic design (Fig. 4O). The diagonal of the 1500×1500 square design matches the diameter of the printing vial (Ø30 mm, corresponding to a row of 2160 mirror units on DMD). The playback has been accelerated and the actual exposure was around 6 minutes. The entire pattern was printed, and the lateral imaging modality captured the inner part of the workpiece.

Movie S4. DTU-SC. The printing process of a 1500×1500 DTU logo using the SC scheme.

Movie S5. DTU-DC-Poly. The printing process of a 1500×1500 DTU logo using the DC-poly scheme.

Movie S6. TL. Side view of the printing process of a 45-floor “twisted torso”. Each floor contains 400 patent compartments. The playback has been accelerated and the printing finished at around the 50th second. The remaining video showcases the architecture by rotating the curing vial without blue or UV illumination.

Movie S7. David. Side view of the printing process of a David bust.

Movie S8. AE. Side view and top view of the printing process of an Albert Einstein bust.

Movie S9. SC-TVP - Processes. Simulated printing process of an arbitrary geometry using single color tomographic printing.

Movie S10. DC-TVP - Processes. Simulated printing process of an arbitrary geometry using dual color tomographic printing, accounting for limited lophyl generation capacity.

Movie S11. DC-TVP - Species. Simulated printing process of an arbitrary geometry using dual color tomographic printing. Evolution of the states of two voxels with different fates.